

ATOMISTIC MODELING PREDICTIONS OF CRACK TIP BEHAVIOR IN
SILICON CARBIDE

A Dissertation

Presented to the Faculty of the Graduate School
of Cornell University

In Partial Fulfillment of the Requirements for the Degree of
Doctor of Philosophy

by

Kai Wing Kelvin Leung

January 2016

© 2016 Kai Wing Kelvin Leung
ALL RIGHTS RESERVED

ATOMISTIC MODELING PREDICTIONS OF CRACK TIP BEHAVIOR IN
SILICON CARBIDE

Kai Wing Kelvin Leung, Ph. D.

Cornell University 2016

This dissertation composes three papers detailing work intended to model the crack tip behavior in silicon carbide (SiC). While having impressive thermal, mechanical, and electrical properties, the utility of SiC as a structural material is often limited by its low fracture toughness. My studies focus on the application of direct molecular dynamics (MD) simulations with empirical potentials, analytic models and electronic structure calculations to illuminate key crack tip mechanisms at low temperature, high temperature and under the influence of impurities. First, I use a multifaceted modeling approach, including electronic structure calculations, MD simulations and analytic models, to illuminate the transition between crack tip mechanisms of single crystal SiC across a range of temperatures and strain rates that govern the intrinsic brittleness of SiC. Then the atomistic predictions are critically examined and compared with published experimental data. The strengths and deficiencies of these analysis tools for predicting crack tip mechanisms in complex covalent materials are discussed in details. Second, I adapt Kohn Sham Density Functional Theory (KSDFT) modeling approach to simulate fracture in SiC under pure mode I and mixed mode loading. In both cases, the crack propagates higher than the Griffith's toughness with a modest lattice trapping effect. Using KSDFT framework to compute the cohesive force across the cleavage plane, the lattice trapping effect as a function mode mixity can be explained. Throughout the work, atomistic simulation predictions are critically compared with published experimental data. Plausible crack tip mechanisms at low temperature and the deficiencies of empirical potential used in MD simulations for predicting crack tip

response in SiC are discussed in detail. Third, I perform a series of KSDFT calculations and atomistic simulations to predict the crack tip behavior in the presence of various impurities at a range of impurity concentration. To mimic the impurity effects on decohesion and slip, a strategic bond shielding approximation is employed by modifying the interactions between the crack tip atoms. Depending on impurity type and concentration, I show that impurities can influence several important crack tip mechanics, including cleavage, dislocation kink nucleation and dislocation kink propagation, that ultimately govern the macroscopic fracture toughness of SiC.

BIOGRAPHICAL SKETCH

Kai Wing Kelvin Leung grew up in Hong Kong, a city in the southern part of China. He graduated from Diocesan Boys' School in his hometown in 2003. He then continued his study at Cornell University in Ithaca NY, with a major in Architecture and a minor in Civil and Infrastructural Engineering. He graduated in 2008, with a Bachelor of Architecture and as a degree marshal of the School of Architecture, Art and Planning. After graduation with his undergraduate degree, he began his graduate study in the School of Civil and Environmental Engineering at Cornell University. In May 2009, he earned his Masters of Engineering degree in Structural Engineering. From 2009 to 2011, he worked as a structural engineer and consultant at Meinhardt C&S Ltd. and AECOM Asia in his hometown. In summer 2011, he joined Professor Derek Warner to begin his graduate research at Cornell University. He earned his Masters of Science in Structural Engineering in January of 2015. In his spare time, Kelvin likes to read, play piano and badminton.

To the whole research group for a friendly research environment and all ideas.

To my family for your love and support.

To Yan Liu, my best friend and the love of my life.

ACKNOWLEDGMENTS

I would first like to thank my advisor, Professor Derek Warner, for his encouragement, patience and useful advice. Second I would like to thank Professors Alan Zehnder, Richard Hennig and Nicholas Zabaras for participating in my graduate committee and inspiring me throughout my time at Cornell. In addition, I gratefully acknowledge support from Ali Sayir at Air Force Office of Scientific Research (Grant No. FA9550-11-1-0273).

TABLE OF CONTENTS

Biographical Sketch.....	iii
Dedication.....	iv
Acknowledgements	v
Table of Contents	vi
1 Introduction	1
2 Atomistic-based Predictions of Crack Tip Behavior in Silicon Carbide across a Range of Temperatures and Strain Rates	3
2.1 Abstract.....	3
2.2 Introduction	3
2.3 Simulation setup	6
2.4 Molecular Dynamics simulation results	10
2.5 Analysis and discussion.....	17
2.6 Summary and conclusion	27
2.7 Acknowledgments	31
3 Kohn-Sham Density Functional Theory Prediction of Fracture in Silicon Carbide under Mixed Mode Loading.....	32
3.1 Abstract.....	32
3.2 Introduction	32
3.3 Modeling methodology and supporting calculations	35
3.4 KSDFT crack tip simulations and analysis	42
3.5 Summary and conclusions	47
3.6 Acknowledgments	48
3.7 Appendix A: computation methodology	48
3.8 Appendix B: computation of cohesive force curves.....	49
3.9 Appendix C: lattice constant, elastic constants and surface energy of the shuffle set of the {111} plane	49
3.10 Appendix D: surface relaxation of the crack plane	51
4 Atomistic Prediction of Impurity Effects on the Intrinsic Brittleness of Silicon Carbide.....	53
4.1 Abstract.....	53
4.2 Introduction	54
4.3 DFT simulation methodology.....	58
4.4 DFT calculation results.....	61
4.5 MD simulation setup	66
4.6 MD simulation results	68
4.7 Summary.....	83
Bibliography.....	85

CHAPTER 1

INTRODUCTION

Over the past few decades, silicon carbide (SiC) has drawn significant attention because of its impressive thermal, mechanical and electronic properties, making it an attractive structural materials for next generation aerospace and semiconductor applications. However, its utility has been limited by its low fracture toughness. To improve its ductility, it is paramount to better illuminate its key crack tip mechanisms that control macroscopic toughness. This dissertation presents a multifaceted approach combining empirical-based molecular dynamics (MD) simulations, analytical models and electronic structure calculations to improve the understanding of atomistic-scale crack tip mechanisms of SiC across a range of temperatures and strain rates. Important SiC crack tip mechanisms including cleavage, lattice trapping, dislocation nucleation and dislocation glide are identified in my study. The final chapter sheds light on the impurity effects on these crack tip mechanisms and fracture toughness of SiC.

The second chapter, entitled “Atomistic-based predictions of crack tip behavior in silicon carbide across a range of temperatures and strain rates” is published in *Acta Materialia*. This work details the use of empirical-based molecular dynamics simulation to simulate the crack tip behavior across a range of temperatures and strain rates. Acknowledging that significant discrepancies may exist between empirical potentials and real SiC material behavior, the simulation results are examined by comparing predictions from analytic models and electronic structure calculations. The strengths and deficiencies of these analysis tools for predicting fracture are discussed in details. This chapter also presents key crack tip mechanisms including cleavage,

dislocation nucleation and glide and argues the brittleness of SiC is not governed by dislocation nucleation, but by dislocation glide.

The third chapter, entitled “Kohn-Sham Density Functional Theory Prediction of Fracture in Silicon Carbide under Mixed Mode Loading” has been submitted to Physical Review B. This work reports the use of Kohn Sham Density Functional Theory calculations to predict the brittle fracture of SiC under pure mode I and mixed mode loading. It shows the crack propagates at a load higher than the Griffith’s toughness, known as the lattice trapping effect. The lattice trapping effect is shown to decrease with mode mixity, which can be explained by the formation of a temporary surface bond during decohesion under shear.

The fourth chapter, entitled “Atomistic prediction of impurity effects on the intrinsic brittleness of silicon carbide”, reports my recent work focusing on understanding the fracture toughness of silicon carbide under the influence of impurities at the crack tip. This study begins with the investigation of the impurity effects on slip and decohesion resistance of a {111} plane using Kohn-Sham Density Functional Theory (KSDFT) calculation. To connect these results with SiC crack tip response, the impurity effects are incorporated into an empirical-based strategic bond shielding approximation approach to reproduce KSDFT trends. The results indicate that the macroscopic fracture toughness is sensitive to the type of impurity and concentration, which control SiC’s key crack tip mechanisms such as decohesion, dislocation kink nucleation and dislocation kink propagation.

CHAPTER 2

**ATOMISTIC-BASED PREDICTIONS OF CRACK TIP BEHAVIOR IN
SILICON CARBIDE ACROSS A RANGE OF TEMPERATURES AND
STRAIN RATES**

By K. W. K. Leung, Z. L. Pan, and D. H. Warner

As published in *Acta Materialia* **77** (2014) 324-334

2.1 Abstract

The utility of silicon carbide (SiC) as an engineering material is often controlled by its brittleness. This work attempts to better illuminate the key mechanisms associated with this property by studying crack tip behavior. A multipronged investigative approach is taken, utilizing direct molecular dynamics simulations with empirical potentials, analytic modeling, and electronic structure calculations. This approach enables us to (1) make atomistic-based predictions of the key mechanisms that occur at a SiC crack tip across a wide range of temperatures and strain rates, and (2) better understand the strengths and deficiencies of these analysis tools for predicting fracture in covalently bonded materials.

2.2 Introduction

Silicon carbide (SiC) has drawn significant attention because of its impressive thermal, mechanical, and electrical properties. It has a high melting temperature, thermal conductivity, stiffness, hardness, electron mobility and a large band gap. SiC resists corrosion and creep, while having a low thermal expansion coefficient and low density. This collection of properties make SiC an attractive material for new technologies that

require high performance in extreme environments [1,2,3,4,5]. However, the utilization of SiC's impressive properties is often hindered by its susceptibility to fracture. This challenge has motivated a long quest to better illuminate the mechanisms that control crack growth in SiC, with the aim of improving mechanical failure prediction and possibly even illuminating new means for improving its fracture resistance.

SiC is brittle at room temperature. Fracture experiments on single crystals report a fracture toughness K_{IC} of 3.2 to 3.3 $\text{MPa}\sqrt{\text{m}}$ [6,7], a value that is larger than the K_{IC} associated with the surface energy, $2.0 \text{ MPa}\sqrt{\text{m}}^*$. While this indicates that surface energy plays an important role in the room temperature K_{IC} of SiC, it also suggests that other energy dissipation mechanisms may be important. TEM observations suggest that small amounts of plasticity may occur near the crack tip, as an increased density of dislocations has been observed near fracture surfaces [8]. This limited room temperature plasticity is thought to involve full dislocations residing on the shuffle set of the close-packed planes [9].

With increasing temperature, plasticity is thought to play a larger role in the fracture and deformation process. At intermediate temperatures 423°K , a significant population of partial dislocations has been observed on the glide set of close-packed planes [10]. While these partial dislocations are thought to be more mobile at elevated temperatures, the macroscopic response of SiC in this temperature range is still brittle. This is attributed to the trailing partial dislocations being largely immobile; and thus, a scenario exists where plastic slip fills the material with stacking faults [11] inhibiting

* Our electronic structure calculations predict a surface energy of $\gamma_s = 4.2 \text{ J/m}^2$ on the close-packed fracture plane, as described in the appendix.

further plasticity. At higher temperatures, the macroscopic response undergoes a brittle to ductile transition (BDT) due to increased mobility of the trailing partial dislocations on the glide set of the close-packed planes. While the BDT temperature depends on strain rate, it is generally reported to occur at a temperature between 1400°K and 2000°K, depending on the specifics of the material and the test [9,12]. The increased mobility of dislocations above the BDT temperature also affects the fracture toughness. For instance, Henshall et al. [6] reported an increase in K_{IC} of slightly more than a factor of $\sqrt{2}$ when the temperature is increased from 1000°K to 1400°K in single crystalline 6H-SiC.

The objective of this manuscript is to report on our investigation into the mechanisms that control crack tip behavior in SiC. Using molecular dynamics (MD) simulations with empirical potentials, we have directly examined the crack tip processes across a range of temperatures and strain rates. The MD simulations revealed a collection of crack tip mechanisms, including cleavage on the {111} plane and dislocation nucleation and glide on the {111} and {100} planes. Acknowledging the brief timescale inherent to MD simulations and inaccuracies in the empirical potentials, a significant disconnect can exist between the MD results and real-world SiC behavior. To address this point, the MD results were examined with simple analytic models and high fidelity electronic structure calculations. This multifaceted modeling approach served to not only illuminate the atomic processes that occur at a crack tip in SiC; but to also establish the utility of a hierarchical modeling approach whereby material parameters, calculated with electronic structure calculations, are fed into popular analytic models to predict crack tip response in SiC.

2.3 Simulation Setup

The orientation of the crack, load, and crystallography can have a significant effect on crack tip response [13]. The orientation studied here was selected following the subsequent line of reasoning. The geometric features of typical engineered structures are large relative to the size and density of microscopic defects in the material. Thus, one can safely assume that the highly stressed regions of a component encompass a population of microscopic material defects. Accordingly, it is then the growth of the most critical microscopic material defect that leads to the formation of a macroscopic crack, ultimately leading to structural failure. Simplifying the material defects to be microscopic cracks, we assume that the important microscopic cracks reside on the low surface energy close-packed planes and the greatest principle stress is normal to the crack plane.

Following this line of reasoning, we began this work by performing MD simulations of 3D 3C-SiC single crystal specimens with a (111) penny crack in their center. Tensile stress was applied normal to the crack plane. Upon reaching a critical load, dislocations nucleated from 3 locations, each having the crack front parallel to $\langle 110 \rangle$ directions, where the crack tip was coincident with the inclined $\{111\}$ planes. Thus, the mode I stress intensity factor (K_I) for dislocation nucleation along these three directions is lower than that for cleavage along all other directions. From this result, we assume that these 3 directions are the most resistant to crack growth, noting that nucleated dislocations shield the crack tip from the applied load and increase the required far-field load for cleavage. Consequently, the overall growth of the penny

crack is controlled by its growth in the $\langle 112 \rangle$ directions of the (111) fracture plane. This follows from the idea that an initially circular crack first grows in the directions with the least crack growth resistance, but the relative driving force in these directions decreases as the crack shape changes. Hence, the growth of the crack in the most resistant directions governs the growth of the embedded crack as a whole [14]. For this reason, this study investigates a (111) through crack with a [1-10] crack front, as this orientation is thought to be key in the development of macroscopic cracks from a population of random defects.

While this work focuses on 3C-SiC, our findings can provide insight into crack tip behavior in other common SiC polytypes such as 4H and 6H. For instance, the close-packed basal plane of the hexagonal polytypes has the same nearest neighbor bonding as the close-packed {111} slip and fracture plane in the 3C structure. Further, Umeno and coworkers [15] have predicted with electronic structure calculations that the ideal shear strength of the basal planes of SiC varies by less than 10% across polytypes.

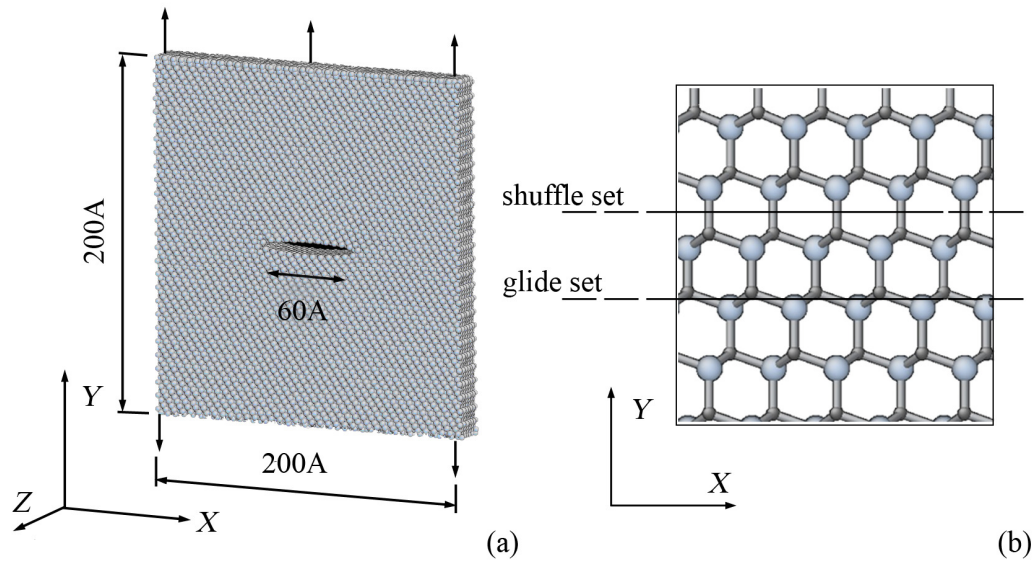


Figure 2.1: (a) MD simulation cell for modeling mode I fracture. (b) depicts the shuffle and glide set of the (111) plane. The X, Y and Z directions correspond to the [11-2], [111] and [1-10] directions of the SiC crystal.

The simulations were conducted on a specimen measuring 200 Å x 200 Å x 20 Å (X x Y x Z) with a 60 Å through crack created by shielding the atomic interaction between atoms above and below the shuffle set of a (111) plane (Figure 2.1). The effect of the specimen size and the exact crack geometry was investigated, by removing a layer of silicon and carbon atoms on the (111) plane rather than shielding atomic interactions. In all cases, the change in the critical K_I was not significant.

Consistent with the previous discussion, the X, Y and Z axes were oriented to the [11-2], [111] and [1-10] directions of the crystal, creating a (111) crack plane and a [1-10] crack front. Traction free boundary conditions were applied in the X and Z directions, while tensile stress was applied in the [111] direction by enforcing an average displacement on the atoms along the Y boundaries of the simulation cell. These boundary conditions create dislocation images forces which encourage dislocation nucleation and glide out of the specimen; although we note that the

boundary induced image force on a nucleating dislocation at a crack tip is negligible due to the geometry of the specimen. The K_{IS} reported for the MD simulations were calculated from the applied tensile stress and crack length, using linear elastic fracture mechanics. Thus, only the K_I values required to initiate the first nonlinear event were subsequently analyzed. Plane stress boundary conditions, as opposed to the more common plane strain atomistic boundary condition [13], were chosen to allow for a wider spectrum of crack tip mechanisms, consistent with the goals of this study. For the modeled orientation, an active (-1-11) glide plane inclines at 70.5° and a (001) plane inclines at 54.7° , with both intersecting the [1-10] crack front.

The simulations were performed using two distinct empirical potentials for comparison, Devanathan et al. [16] and Erhart and Albe [17]. The Devanathan et al. potential is an improved version of Tersoff's original SiC potential [18], which attempts to reproduce the lattice and elastic constants, cohesion energy, point defect formation energies and short range interatomic repulsion. The Erhart and Albe potential was designed to apply to a large configuration space, involving multiple phases, reproducing lattice and elastic constants, cohesion energy and point defect formation energies. To better understand the temperature dependent performance of these potentials, we calculated the melting temperature with direct MD simulation and obtained 4990°K for the Devanathan et al. potential and 4490°K for Erhart and Albe potential. These values are significantly higher than the experimentally observed melting temperature of 3100°K [19], but consistent with the phase transformation temperature of the Tersoff potential [20]. The ability of these potentials to reproduce

surface energies and unstable stacking fault energies is presented in the analysis and discussion section.

The mode I fracture simulations were conducted with the LAMMPS package [21]. The temperature was controlled by a Langevin thermostat with a damping parameter of 0.15 ps [22]. As dislocation activity is sensitive to thermal activation [6,23], 6 temperatures between 10°K and 1000°K were examined at three applied \dot{K}_I s (5×10^8 MPa $\sqrt{\text{m/s}}$, 5×10^9 MPa $\sqrt{\text{m/s}}$ and 5×10^{10} MPa $\sqrt{\text{m/s}}$). The 1000°K upper limit of the temperature range was chosen because SiC oxidizes rapidly above $\sim 1100^\circ\text{K}$, forming a silica surface layer [1]. A converged time integration step of 2 fs was used. Strains were computed from the prescribed displacements at the boundaries and stresses were computed with the virial theorem. Visualization was performed with the Atomeye package [24].

2.4 Molecular Dynamics Simulation Results

Across the range of temperatures and \dot{K}_I s examined, both cleavage and dislocation nucleation were observed as shown in Figure 2. At the lowest temperatures, cleavage was dominant for the Devanathan et al. potential and dislocation nucleation was observed for the Erhart and Albe potential. For the Devanathan et al. potential (below 600°K at $\dot{K}_I = 5 \times 10^8$ MPa $\sqrt{\text{m/s}}$ and 5×10^9 MPa $\sqrt{\text{m/s}}$, and below 800°K at $\dot{K}_I = 5 \times 10^{10}$ MPa $\sqrt{\text{m/s}}$) the crack initiated on the shuffle set of the (111) plane, in the [11-2] direction (Figure 2.3), consistent with the relatively low surface energy of this plane. Propagation created a rough fracture surface, disordering atomic packing within a few atomic planes of the surface.

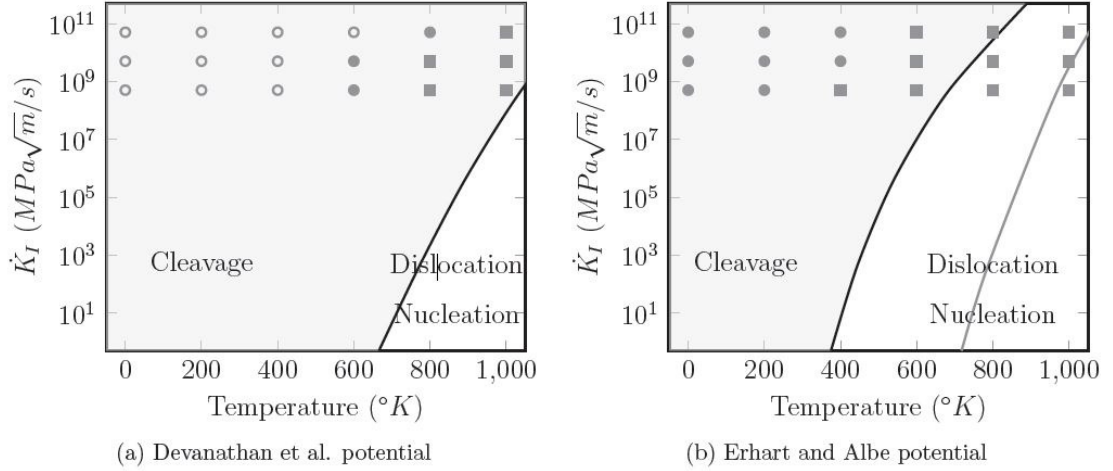


Figure 2.2: Crack tip mechanism map of the MD simulations represented by gray data points: Open circles represent cleavage on the $\{111\}$ plane; filled circles represent dislocation nucleation on the $\{111\}$ plane; squares represent dislocation nucleation on the $\{100\}$ and $\{111\}$ planes. Analytic model predictions of the crack tip mechanism: black curve represents transition from cleavage on the $\{111\}$ plane to dislocation nucleation on the $\{111\}$ plane; gray curve represents transition from cleavage on the $\{111\}$ plane to dislocation nucleation on the $\{100\}$ plane. Cleavage regime is shaded in light gray.

With the Erhart and Albe potential, dislocation nucleation was found to be the first crack tip mechanism at the lowest temperature for all K_I s examined. A leading partial, with Si-Si core structure, nucleated on the glide set of the inclined $(-1-11)$ plane from the right side of the crack. Due to high glide resistance at low temperature, the partial dislocation was trapped at the crack tip. Bond rupture was then observed on the horizontal (111) shuffle plane in the $[11-2]$ direction followed by opening and sliding along the inclined $(-1-11)$ plane (Figure 2.4). Considering the short-range character of the Erhart and Albe potential and the atomistic analysis of fracture in covalent materials by Mattoni et al. [25] and Sinclair [26], we note that the propagation of the crack on an inclined plane may be an artifact of unphysically large debonding force in the potential. Contrary to the Devanathan et al. potential, the fracture surface was atomically sharp.

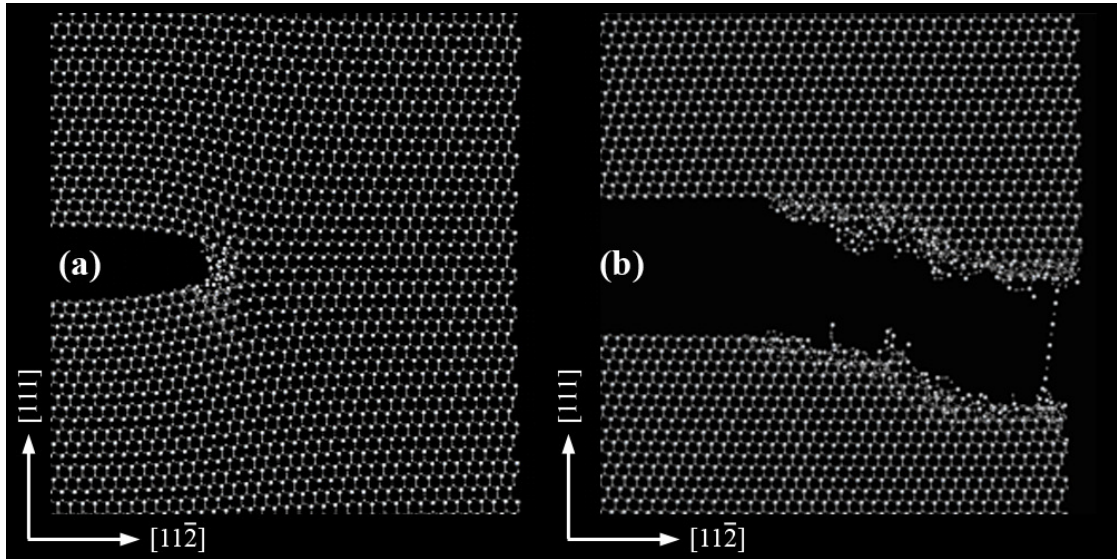


Figure 2.3: Cleavage with the Devanathan et al. potential at 10°K and $\dot{K}_I = 5 \times 10^8 \text{MPa}\sqrt{\text{m/s}}$. Image (a) corresponds to the atomic configuration at $K_I=2.90 \text{MPa}\sqrt{\text{m}}$. Note the atomic rearrangement close to the crack tip on the shuffle set of the (111) plane, which was not observed prior to this load. Image (b) corresponds to the atomic configuration after catastrophic crack propagation at $K_{IC}=3.52 \text{MPa}\sqrt{\text{m}}$.

Figure 2.5 gives the K_I at which cleavage occurred in the simulations for the Devanathan et al. potential. Considering that the experimentally measured value of K_{IC} for single crystalline SiC at room temperature is $\sim 3.3 \text{MPa}\sqrt{\text{m}}$ [6,7], the MD simulations are in excellent agreement. However, as will be discussed in the following section, we believe that this close agreement with experiments is primarily the result of a coincidental cancellation of errors occurring in the empirical potential.

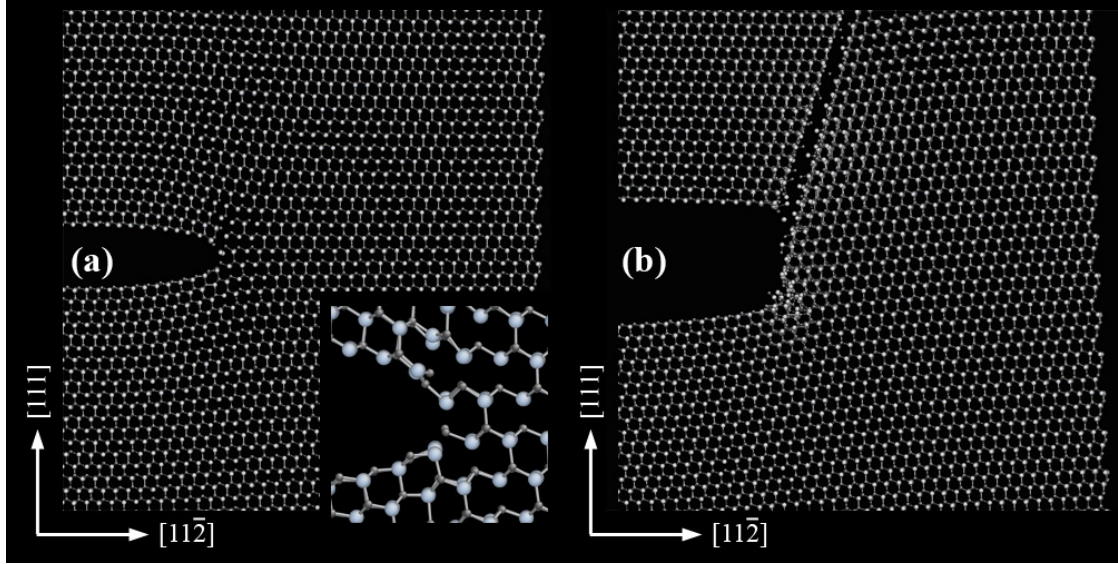


Figure 2.4: Dislocation nucleation with the Erhart and Albe potential at 10°K and $\dot{K}_I = 5 \times 10^8 \text{MPa}\sqrt{\text{m}}/\text{s}$. Image (a) shows the dislocation nucleated on the (-1-11) plane with Si-Si core structure (inset) on the right side of the crack tip at $K_I = 2.39 \text{MPa}\sqrt{\text{m}}$. Image (b) shows the specimen immediately after catastrophic failure due to cleavage on the shuffle set of the inclined (-1-11) plane at $K_{IC} = 3.20 \text{MPa}\sqrt{\text{m}}$.

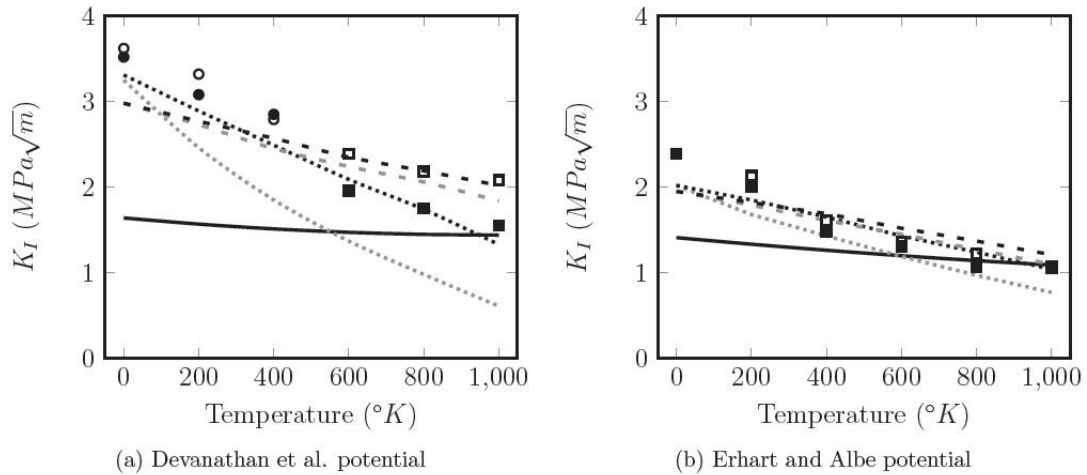


Figure 2.5: The critical SIF for cleavage (K_{IC}) and the SIF for dislocation nucleation (K_{IN}) as a function of temperature for the MD simulation results: circles represent cleavage on the $\{111\}$ plane; squares represent dislocation nucleation on the $\{111\}$ plane. Filled symbols represent $\dot{K}_I = 5 \times 10^8 \text{MPa}\sqrt{\text{m}}/\text{s}$; open symbols represent $\dot{K}_I = 5 \times 10^{10} \text{MPa}\sqrt{\text{m}}/\text{s}$. The analytic results are plotted for comparison: solid curve represents $K_{IC\{111\}}$; black dotted curve represents $K_{IN\{111\}}$ at $\dot{K}_I = 5 \times 10^8 \text{MPa}\sqrt{\text{m}}/\text{s}$; black dashed curve represents $K_{IN\{100\}}$ at $\dot{K}_I = 5 \times 10^8 \text{MPa}\sqrt{\text{m}}/\text{s}$; gray dotted curve

represents $K_{IN\{111\}}$ at $\dot{K}_I = 5 \times 10^{-1} \text{MPa}\sqrt{\text{m/s}}$; gray dashed curve represents $K_{IN\{100\}}$ at $\dot{K}_I = 5 \times 10^{-1} \text{MPa}\sqrt{\text{m/s}}$.

At intermediate temperatures, dislocation nucleation was the initial irreversible event to occur. In both cases it occurred on the right side of the crack (Figure 2.1) at K_I shown in Figure 2.5. For the Devanathan et al. potential (at 600°K and $\dot{K}_I = 5 \times 10^8 \text{MPa}\sqrt{\text{m/s}}$ and $\dot{K}_I = 5 \times 10^9 \text{MPa}\sqrt{\text{m/s}}$, and above 800°K for all \dot{K}_I s), a partial dislocation nucleated on the glide set of the inclined (-1-11) plane as shown in Figure 2.6. Dislocation nucleation on the glide set of a close-packed plane is consistent with MD simulation results of SiC and silicon in the literature [13,27]. The core structure of the nucleated partial dislocation contained Si-Si bonds. This observation is consistent with the experimental deduction that partial dislocations with a Si-Si core structure are more mobile than those with a C-C core structure [28,29]. Nonetheless, the motion of the Si-Si partial dislocation was limited, as it remained close to the crack tip. As the load was further increased, the crack grew by a small amount. A full dislocation then nucleated on the shuffle set of the inclined (-1-11) plane and glided to a distance of ~60Å from the crack tip, shortly before the onset of cleavage. The crack propagated on the shuffle set of the horizontal (111) plane in the [11-2] direction, similar to the lower temperature cases.

For higher temperatures, up to 1000°K, with the Devanathan et al. potential, dislocation nucleation also occurred on the left side [-1-12] of the crack. Nucleation occurred on the inclined (00-1) plane with a slip direction of [110], and the dislocation glided to a distance of ~40Å from the crack tip (Figure 2.6). After nucleation of a

single dislocation on this plane and under the continued increase of applied load, the crack eventually propagated on an inclined plane.

With the Erhart and Albe potential, dislocation nucleation and glide occurred in all simulations at and above 400°K and for all examined \dot{K}_I s. As seen in Figure 2.5, dislocation nucleation occurred at a lower load than with the Devanathan et al. potential. A leading partial, with Si-Si core structure, nucleated on the glide set of the inclined (-1-11) plane, similar to the lower temperature cases. With increasing load, the corresponding trailing partial dislocation with C-C core structure then nucleated. Unlike the low temperature cases, the dissociated dislocation moved quickly to the free surface of the specimen. In no cases was crack tip twinning observed. At $\dot{K}_I = 5 \times 10^8 \text{MPa}\sqrt{\text{m/s}}$ at 400°K and at all \dot{K}_I s at higher temperatures, full [-1-10] dislocation nucleation on the (001) plane occurred on the right side of the crack. These dislocations were more mobile than with the Devanathan et al. potential simulations, gliding to the free surface (Figure 2.7). With the Erhart and Albe potential, the glide of the nucleated dislocations to the free surface of the specimen allowed for continued dislocation nucleation from both sides of the crack as the load was increased, significantly delaying crack propagation.

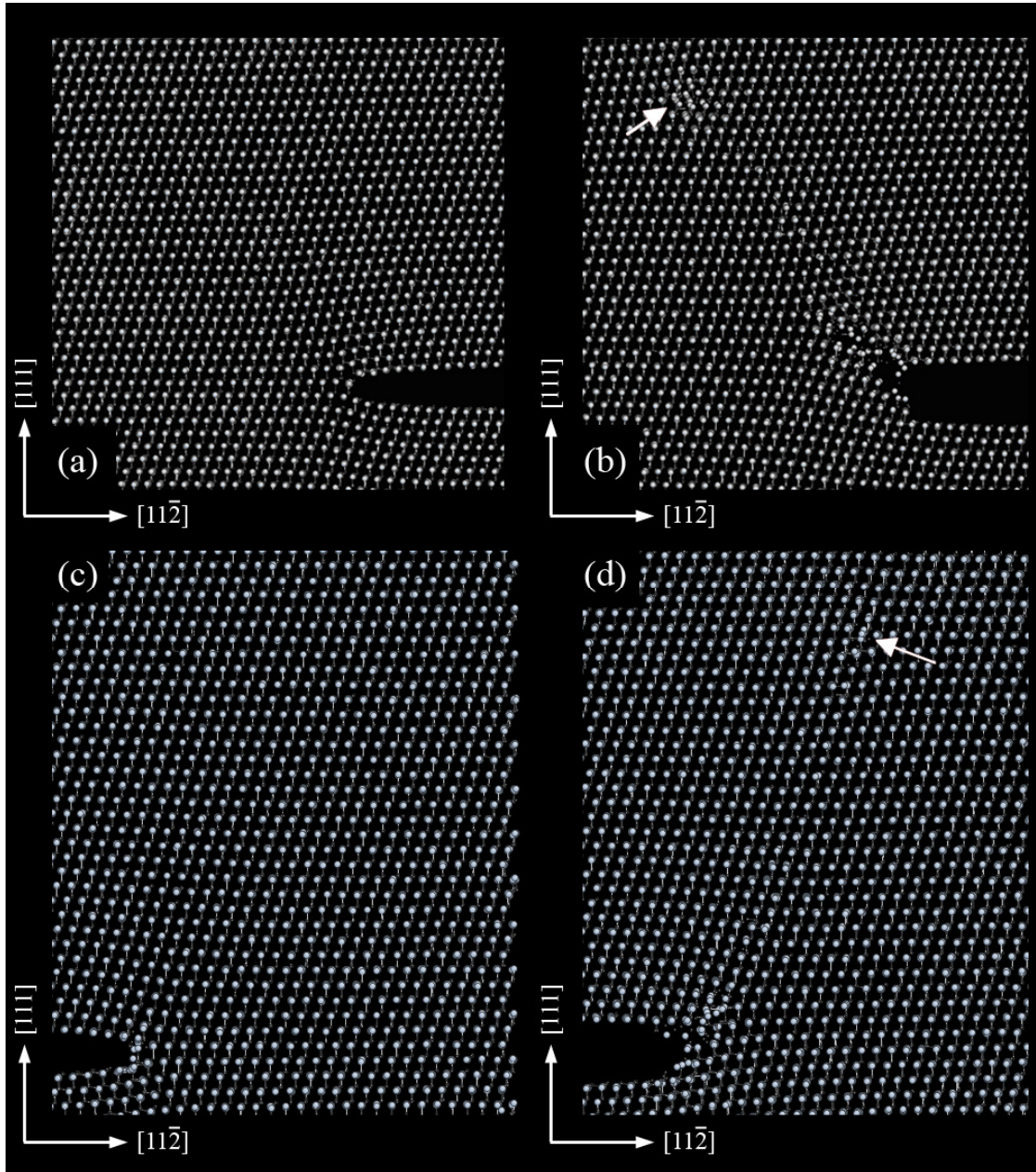


Figure 2.6: Dislocation nucleation with the Devanathan et al. potential at temperature = 1000°K and $\dot{K}_I = 5 \times 10^8 \text{MPa}\sqrt{\text{m/s}}$. The crack tip responded plasticity by dislocation nucleation on the (-1-11) plane on the right side and on the (00-1) plane on the left side of the crack. Image (a) shows the atomic configuration at the crack tip immediately after dislocation nucleation on the (00-1) plane on the [-1-12] crack side and image (b) shows the dislocation was trapped at a distance of ~40Å from the crack tip indicated by the arrow. Image (c) shows dislocation nucleation with leading partial on the (-1-11) plane on the [11-2] crack side at $K_I=1.55\text{MPa}\sqrt{\text{m}}$ and image (d) shows the full dislocation was trapped at a distance of ~60Å from the crack tip indicated by the arrow. Both dislocations were trapped in the bulk near the crack tip due to high glide resistance. The crack then propagated as the load was increased.

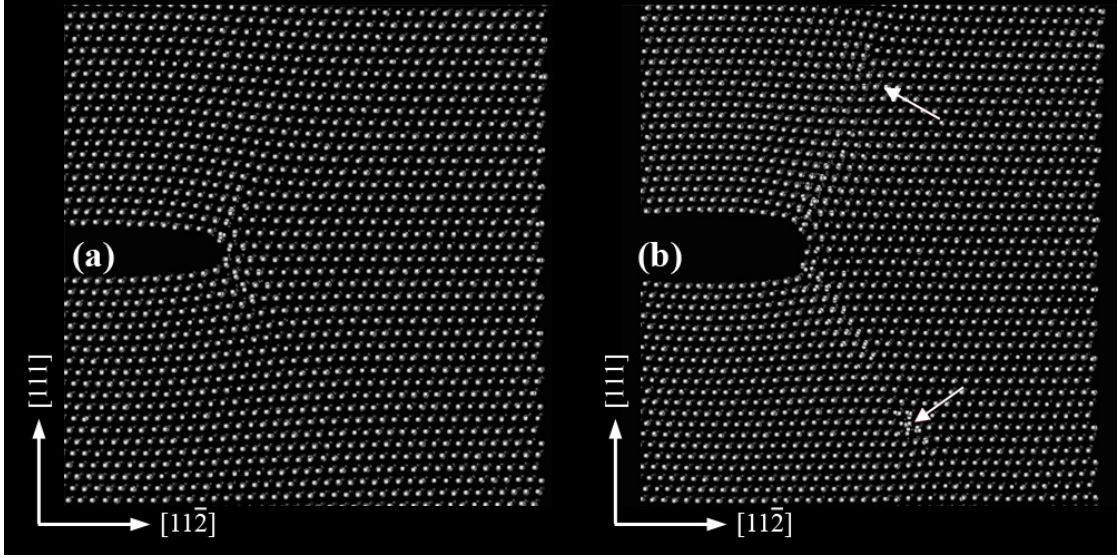


Figure 2.7: Dislocation nucleation with the Erhart and Albe potential at 400°K at $\dot{K}_I = 5 \times 10^8 \text{MPa}\sqrt{\text{m}}/\text{s}$. The crack tip responded plastically by nucleating dislocations on both the $\{111\}$ and $\{100\}$ planes for both crack sides. Image (a) shows the atomic configuration at the crack tip immediately after dislocation nucleation at $K_I = 1.48 \text{MPa}\sqrt{\text{m}}$ and image (b) shows the crack tip configuration at $K_I = 2.27 \text{MPa}\sqrt{\text{m}}$ where the dislocations have glided away from the crack tip into the crystal. The arrow above the crack tip indicates the full dislocation with leading partial and trailing partial nucleated on the inclined $(-1-11)$ plane. The arrow below the crack tip indicates the full dislocation on the (001) plane.

2.5 Analysis and Discussion

Given a sufficient separation of length scales, $K_I > K_{IC}$ is an accurate and general criterion for mode I crack growth. Here we consider Griffith's widely used analytic model [30], whereby crack growth occurs when it is thermodynamically favorable, i.e.

$K_{IC} = \sqrt{2\gamma_s E^*}$ for plane strain condition[†]. γ_s represents the surface energy of the fracture plane and E^* represents the appropriate elastic constant. For the material anisotropy and orientation of the specimen considered here,

[†] We remind the reader that the MD simulations were performed in plane stress, whereas the analytical model was formulated in plane strain for convenience. The difference in the predicted critical K_I values between these two conditions is represented by the factor $\sqrt{1-\nu^2}$ which is insignificant for SiC, considering its low value of ν (Voigt averaged Poisson's ratio).

$$E^* = \left(\frac{S_{11}}{2} \sqrt{1 + \frac{2S_{12} + S_{66}}{2S_{11}}} \right)^{-1} \quad (2.1)$$

with the S_{ij} being the components of the compliance matrix in the linear elastic limit of the crack system.

E^* and γ_s have been calculated across a range of temperatures for both of the empirical potentials used in the MD simulations. As shown in Figure 2.8, the elastic constants are found to be relatively independent of temperature over the range investigated, and to be in reasonable agreement with experimental values [31,32] and electronic structure calculations at 0°K, carried out using Kohn-Sham Density Functional Theory (DFT) as described in the appendix.

The surface energy corresponding to the fracture plane in the MD simulations ({111} shuffle set) is shown in Figure 2.9 for both potentials. To appropriately connect with Griffith's crack propagation criterion, the surface energy reported here is the average of the C and Si terminated surfaces. It is found to be temperature dependent, decreasing linearly with temperature by 21% and 38%, respectively for the Devanathan et al. and Erhart and Albe potential, over the temperature range examined. As can be seen from Figure 2.9, the temperature dependence is largely due to the entropic contribution to the free energy. The values of the 0°K surface energy for both potentials can be compared to two reference points. First, the surface energy values of other SiC empirical potentials yield values between 1.3-2.3 J/m² [13]. Second, our DFT calculations predict a value of 4.2 J/m² for the average surface energy of the C and Si terminated ideal surfaces.

Using the values of the relevant elastic constants and surface energy, Griffith's model predicts $K_{IC}=1.68 \text{ MPa}\sqrt{\text{m}}$ and $K_{IC}=1.38 \text{ MPa}\sqrt{\text{m}}$ for the Devanathan et al. potential and the Erhart and Albe potential respectively. These values are significantly below the predictions from the MD simulations for both potentials. For the Devanathan et al. potential, this conclusion is directly evident (Figure 2.5). However, for the Erhart and Albe potential, the atomistic simulations only bound K_{IC} to be above $K_I=2.39 \text{ MPa}\sqrt{\text{m}}$, i.e. the value at which a leading partial dislocation nucleated.

Considering that Griffith's model is exact in the thermodynamic limit of cleavage, the difference between the model and the MD simulations suggests that kinetic barriers, such as lattice trapping, significantly inhibited crack growth in the MD simulations for both potentials [33,34]. For the Devanathan et al. potential, the role of lattice trapping remains significant up to the cleavage to dislocation nucleation transition temperature, delaying crack propagation.

Noting that (1) lattice trapping is generally thought to be artificially large in empirical potential models of covalent solids [25,33], and (2) the potentials significantly under-predict the surface energy of the fracture plane relative to DFT predictions, it is reasonable to conclude that the artificial effects of (1) and (2) offset each other such that the K_{IC} obtained in the MD simulations is in close agreement with experimental values.

To analytically model the dislocation nucleation process, the energetics of the process must be considered from a kinetics perspective since dislocation nucleation often leads to a lower energy state, even at low loads. Under constant \dot{K}_I and temperature, the most probable stress intensity factor (SIF) for dislocation nucleation,

K_{IN}^p meaningfully characterizes the nucleation process on a particular slip system. The value of K_{IN}^p is obtained numerically by finding the value of K_I that satisfies the equality [35]

$$\frac{Q_{3D}(K_I)}{k_B T} = \ln \left(\frac{k_B T N \omega_0}{\dot{K}_I \Omega(K_I)} \right) \quad (2.2)$$

where Q_{3D} is the activation energy barrier for dislocation nucleation at finite temperature, k_B is Boltzmann's constant, and T is the temperature. $N\omega_0$ represents the number of potential nucleation sites along the crack front multiplied by the attempt frequency at the equilibrium state. \dot{K}_I represents the loading rate of the K_I and captures the timescale effect. Ω is the activation volume defined by $\Omega = -d Q_{3D}/d K_I$.

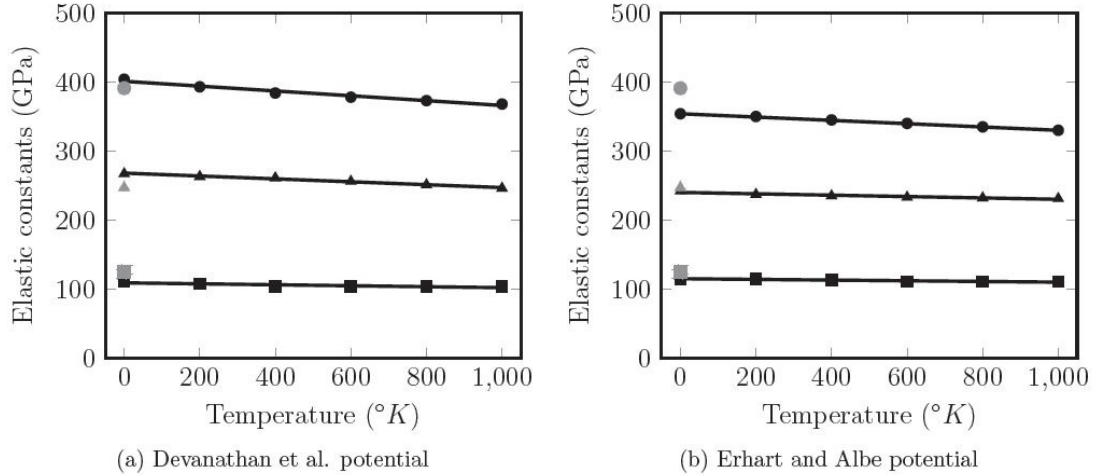


Figure 2.8: Elastic constants as a function of temperature from 0°K to 1000°K: circles represent C_{11} ; squares represent C_{12} ; triangles represent C_{44} . Black symbols represent empirical potentials; gray symbols represent DFT.

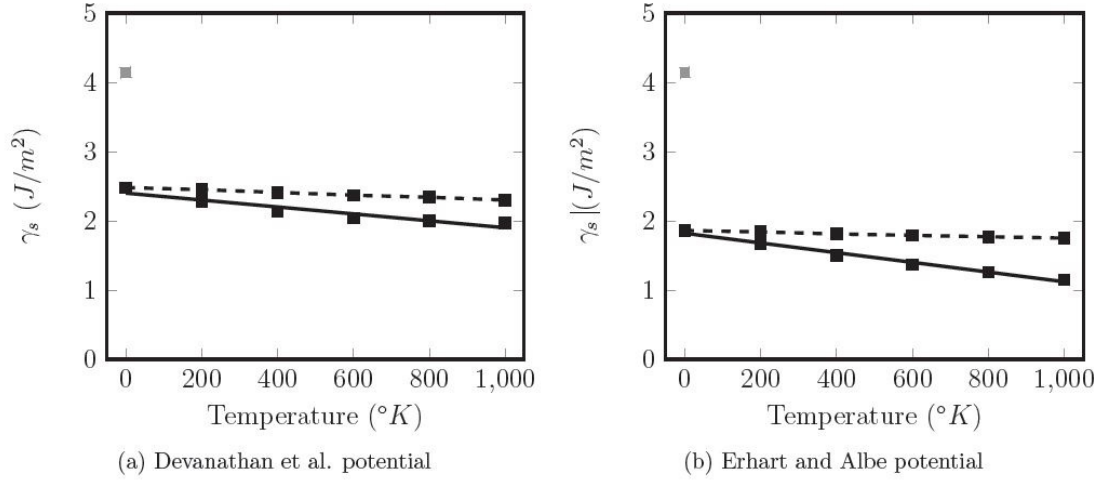


Figure 2.9: {111} shuffle plane surface energy (average surface energy of the C and Si terminated surfaces) as a function of temperature from 0°K to 1000°K: solid curve represents free energy; dashed curve represents enthalpy; gray squares represent DFT.

Taking a first order approximation of the shape of the energy barrier near the critical load, the activation energy barrier can be expressed as a function of the ratio between the applied SIF and critical SIF for dislocation nucleation on the slip plane [23]. To account for crystal anisotropy, the expression was modified by replacing the energy factor $\mu/(1-\nu)$ for an isotropic medium by H defined in [36], given by

$$Q_{3D} = 1.435b^3 H \left(1 - \frac{K_{II}^{eff}}{K_{IIN}^{eff}} \right)^{\frac{3}{2}} \quad (2.3)$$

In equation 2.3, b is the magnitude of the Burgers vector of the slip system, and H is an energy factor [36] that is dependent on the anisotropic elastic constants and the geometry of the slip system. K_{IIN}^{eff} is the critical mode II SIF required for dislocation nucleation in the absence of thermal activation. Following [23] and [36],

K_{IIN}^{eff} and K_{II}^{eff} are taken as

$$K_{IIN}^{eff} = \sqrt{2H(\cos^2 \phi + (1-\nu) \sin^2 \phi) \gamma_{us}} \quad (2.4)$$

and

$$K_{II}^{eff} = K_I \cos^2\left(\frac{\theta}{2}\right) \sin\left(\frac{\theta}{2}\right) \cos\phi \quad (2.5)$$

with γ_{us} being the unstable stacking fault energy, θ the inclination angle of the slip plane, and ϕ the out-of-plane angle of the Burgers vector.

Here, N_{00} is taken to be $3 \times 10^{12}/s$, consistent with similar works [37]. Q_{3D} is a function of the applied load, the elastic constants, γ_{us} , and the geometry. Noting that the elastic constants and γ_{us} depend on the temperature, Q_{3D} is also temperature dependent, a point that has been highlighted recently in the literature [38,39,40,41]. For dislocation nucleation on the right side of the crack, nucleation on the (001) and (-

1-11) planes have been considered. For the (001) plane and lattice constant a , $b = \frac{a}{\sqrt{2}}$,

$$\phi = 0^\circ, \quad \theta = 54.7^\circ, \quad \text{and} \quad H = (\bar{C}_{12} + C_{12}) \sqrt{\frac{C_{66}(\bar{C}_{12} - C_{12})}{C_{22}(\bar{C}_{12} + C_{12} + 2C_{66})}}, \quad \text{where} \quad \bar{C}_{12} = \sqrt{C_{11}C_{22}}$$

in the coordinate system given in [36]. For the (-1-11) plane, $b = \frac{a}{\sqrt{6}}$, $\phi = 0^\circ$,

$$\theta = 70.5^\circ, \quad \text{and} \quad H = \left(\frac{C + C_{12}}{3}\right) \left(1 + \frac{2C_{11}}{C}\right) \sqrt{\frac{C_{44}(C - C_{12})}{C_{11}(C + C_{12} + 2C_{44})}}, \quad \text{where}$$

$$C = \sqrt{\frac{(C_{11} + C_{12} + 2C_{44})C_{11}}{2}} \quad \text{in the simple cubic coordinate system.}$$

γ_{us} was computed for both potentials for all of the cases of dislocation nucleation observed in the MD simulations, i.e. $\langle 110 \rangle$ slip on the $\{100\}$ plane, $\langle 110 \rangle$ slip on the shuffle set of the $\{111\}$ plane, and $\langle 112 \rangle$ slip on the glide set of the $\{111\}$ plane. The last case corresponds to the formation of a partial dislocation, with both the

leading and trailing partial having the same value of γ_{us} . Thus, it is important to point out that the analytic model does not distinguish between the relaxed partial dislocation core structures observed in the MD simulations. The temperature dependence of γ_{us} was plotted for both potentials for dislocation nucleation on the glide set of the $\{111\}$ plane and slip on the $\{100\}$ plane (Figure 2.10). In all cases, γ_{us} decreases with temperature in an approximately linear fashion, with the temperature dependence being largely driven by entropic effects.

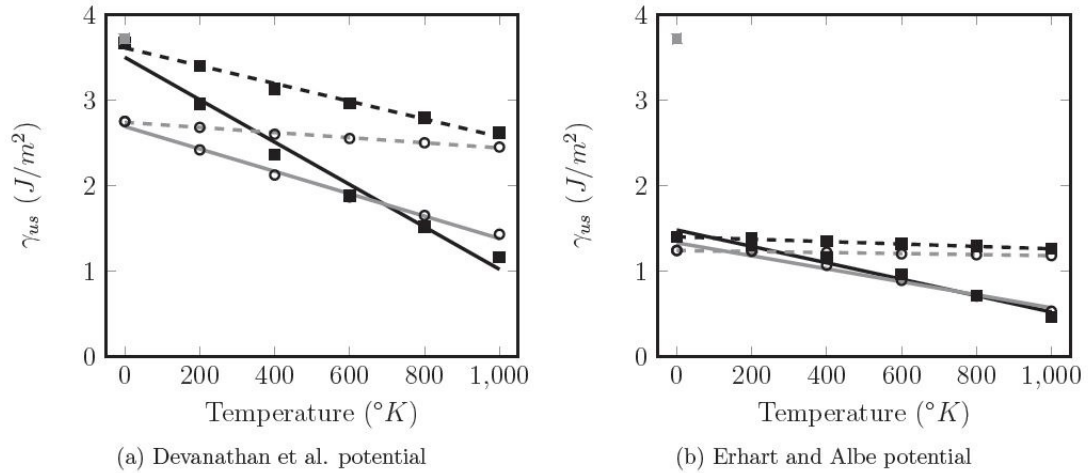


Figure 2.10: Unstable stacking fault energies (γ_{us}) of the $\{111\}$ glide and $\{100\}$ planes as a function of temperature from 0°K to 1000°K: dashed black curve represents $\{111\}$ enthalpy; solid black curve represents $\{111\}$ free energy; dashed gray curve represents $\{100\}$ enthalpy; solid gray curve represents $\{100\}$ free energy; gray squares represent $\{111\}$ DFT.

The first irreversible event to occur in the MD simulations at elevated temperatures was partial dislocation nucleation from the right side of the crack on the inclined $(-1-11)$ plane. Accordingly, the K_I at which this event occurred in the simulations can be directly compared to the analytic model predictions of K_{IV}^p . Using the temperature dependent values of γ_{us} and the elastic constants, the analytic model predictions for both potentials are found to be in close agreement with the MD

simulation results above 600°K. With the Erhart and Albe potential, the analytic model agreement is less at temperatures lower than 400°K, with the analytic model predictions underestimating K_{IN}^p relative to the MD simulation results (Figure 2.5).

K_{IN}^p decreases with increasing temperature due to its dependence on the thermal energy available for activation and the temperature dependence of Q_{3D} . K_{IN}^p 's temperature dependence is stronger than that of K_{IC} , which drives the transition from cleavage to dislocation nucleation with increasing temperature, consistent with the MD simulation results. With both potentials, the analytic model predicts a transition temperature above what was observed in the MD simulations. This is directly attributed to the low value of K_{IC} in the analytic model relative to its observed value in the MD simulations, a result of the lattice trapping effect.

Considering all the observed plastic slip scenarios in the MD simulations for the Devanathan et al. potential, the analytic model predicts dislocation nucleation on the (001) from the right side of the crack to be the most favorable mechanism at low temperatures (Figure 2.5). However, due to K_{IN}^p for dislocation nucleation on the (001) plane decreasing more slowly with temperature than that on the (-1-11) plane, the analytic model predicts a cross-over exists in the preferred nucleation mechanism with increasing temperature. This cross-over in preferred nucleation mechanisms occurs while cleavage is still the overall preferred mechanism, and thus dislocation nucleation on the (001) plane at lower temperatures is never predicted, in accordance with the MD simulation results. At higher temperatures, the model predicts dislocation nucleation on the (-1-11) plane to be the preferred mechanism for the initial plastic

slip event, which is again consistent with the MD simulation results. For the Erhart and Albe potential at low temperature, the analytic model predicts cleavage on the horizontal (111) plane, however, due to lattice trapping, cleavage on this plane was suppressed and dislocations nucleated on the (001) and (-1-11) plane. As shown in Figure 2.5, K_{IN}^p for dislocation nucleation on the (001) plane is similar to that on the (-1-11) plane at high temperature. Hence, the analytic model predicts both dislocation events are likely at high temperature, consistent with the MD simulation results.

While full dislocation nucleation on the shuffle set of the {111} plane is thought to occur in experiments at lower temperatures [9], the value of γ_{us} for this slip system at 0°K was found to be very large relative to the γ_{us} of the glide set of the {111} plane and the {100} plane. Specifically, $\gamma_{us} = 6.51 \text{ J/m}^2$ for the Devanathan et al. potential and $\gamma_{us} = 6.72 \text{ J/m}^2$ for the Erhart and Albe potential. However, these values are not consistent with DFT calculations, $\gamma_{us} = 3.95 \text{ J/m}^2$, suggesting that it is deficiencies in the empirical potentials that are responsible for the disconnect between experiments and predictions from the analytic model and MD simulations. Alternatively, the 0°K γ_{us} value for <110> slip on the {100} plane appears to be under predicted by both empirical potentials, with the DFT calculations giving $\gamma_{us} = 7.57 \text{ J/m}^2$ (Figure 2.10). The occurrence of dislocation nucleation on the {100} plane may also be an artifact of the empirical potentials.

For the most commonly observed slip case, <112> slip on the glide set of the {111} plane, the value of γ_{us} at 0°K for the two potentials differs significantly, with the value from the Devanathan et al. potential being very close to the DFT predictions of 3.72 J/m^2 . The difference in γ_{us} between the two potentials is consistent with

dislocation nucleation occurring at lower loads on this slip system for the Erhart and Albe potential, in both the MD simulations and analytic model.

Considering (A) the above comparisons of γ_{us} for the various slip systems, empirical potentials, and DFT predictions; (B) that the analytic model and MD simulations agree in their predictions of dislocation nucleation loads across the range of temperatures; and (C) that predictions of K_{IC} using the Devanathan et al. potential correspond closely with experiment; the following assertions can be made regarding the competition of mechanisms observed in the MD simulations: (1) With the Devanathan et al. potential, the competition between cleavage and dislocation nucleation on the glide set of the (-1-11) plane is likely to be representative of real SiC behavior. (2) The (00-1) slip at the crack tip predicted by the models is probably unrealistic, as slip on this system is likely due to inaccuracies in the empirical potentials relative to real SiC. (3) Contrarily, slip on the shuffle set of the (-1-11) plane is artificially difficult in the empirical potential based models. While this suggests the operation of an additional plastic slip mechanism beyond those readily observed in the MD simulations, it is not clear that this mechanism would have a significant qualitative effect on crack tip behavior, as it occurs on a slip plane that is already active. Quantitatively, it could push the transition from cleavage to dislocation nucleation at the crack tip towards higher \dot{K}_I s and colder temperatures.

Assembling all pieces of this work, we hypothesize that a transition from cleavage to dislocation nucleation occurs at the crack tips of the most important defects in SiC at a temperature in the neighborhood of 300°K, or less, at typical experimental strain rates (10^{-2} /s). We base this hypothesis off of shifting the analytic

model predictions for the Devanathan et al. potential to lower temperatures to make them consistent with the MD simulations results (Figure 2.2). Considering that this value is well below the experimentally observed BDT temperature, these results are consistent with the idea that the BDT transition temperature is not controlled by dislocation nucleation from sources, but by dislocation mobility. This assertion is in accordance with experimental observations of dislocations near the surface of specimens fractured at room temperature [8], and observations of a relatively constant single crystal fracture toughness between room temperature and 873°K [6]. Finally, we point out that although the transition in crack tip response from cleavage to dislocation nucleation is likely not the controlling condition of the BDT, it is a necessary condition [42,43].

2.6 Summary and Conclusion

In summary, this work sought to increase the understanding of crack tip behavior in SiC across a range of strain rates and temperatures. The work began with the selection of an important crack configuration for study. An attempt was made to select a configuration that is likely to govern the ultimate strength of a macroscopic SiC component under load. Following linear elastic continuum analysis and MD simulations of a 3D penny cracks, a through crack on a (111) plane with a [1-10] crack front was selected.

Direct empirical potential based MD simulations were performed on this configuration. Realizing that significant discrepancies often exist between empirical potentials and real material behavior, especially for covalently bonded materials, two distinct SiC potentials were studied. A wide range of crack tip mechanisms were

observed in the simulations, with the response being particularly dependent on the temperature and strain rate at which the simulation was conducted. At lower temperatures, crack propagation on the (111) crack plane was observed; while at higher temperatures, partial dislocation nucleation on the glide set of the inclined (-1-11) plane occurred. Both of these responses are consistent with experimental observation. Further, the observed K_{IC} in the MD simulations is in close agreement with experimental measurements of K_{IC} in single crystalline SiC at room temperature.

SiC crack tip mechanisms not reported in the experimental literature were also observed in the MD simulations, including dislocation nucleation on the (00-1) planes and crack turning onto an inclined (-1-11) plane from a mode I loaded (111) plane. Contrastingly, several mechanisms reported in the literature were not readily observed in the simulations, including dislocation nucleation on the shuffle set of the (-1-11) plane and dislocation nucleation on the glide set of the (-1-11) plane with only leading partial and stacking fault [11].

The crack tip mechanisms were then analyzed with Griffith's linear elastic crack propagation model and a crack tip dislocation nucleation model built upon the works of Peierls, Rice, Beltz, and Zhu [23,44,45,35]. Acknowledging the importance of temperature dependent material parameters in these models, the elastic constants, surface free energies, and relevant unstable stacking fault free energies were calculated over a range of temperatures for both potentials using both direct MD simulation and thermodynamics integration method. These calculations showed the importance of the entropic component of the free energy for both surfaces and stacking faults in SiC.

The analytic model predictions for cleavage and crack tip dislocation nucleation were then compared to the MD results. In all cases a transition from cleavage to dislocation nucleation with increasing temperature was observed. In the case of cleavage, Griffith's model predictions of K_{IC} were significantly below the values obtained in the MD simulations. This discrepancy is attributed to the existence of a large lattice trapping barrier to crack growth with the empirical potentials. Considering the low surface energies of the potentials together with the close agreement between the MD crack growth predictions and experiment, the large lattice trapping barrier of the potentials appears to be artificial. For dislocation nucleation, the analytic model predictions agreed reasonably with the MD simulations for the investigated temperature ranges for both potentials, with both models predicting K_I decreasing linearly with increasing temperature. However, the analytic model predicts the transition from cleavage to dislocation nucleation at higher temperatures relative to the MD simulation results. These predictions could be improved by incorporating the lattice trapping effect in the cleavage model.

With an increased understanding of the accuracy of the analytic models to predict crack tip behavior in SiC, the accuracy of the empirical potentials was examined by inspecting the key material parameters that control crack tip behavior. Taking DFT predictions of these parameters to be in accordance with real SiC, it seems that both empirical potentials likely over predict the occurrence of slip on the $\{100\}$ plane and under predict the occurrence of slip on the shuffle set of the $\{111\}$ plane. For the Devanathan et al. potential, the value of γ_{us} for partial dislocation nucleation on the glide set of the $\{111\}$ plane was found to correspond well with DFT

predictions. This suggests that the transition from cleavage to dislocation nucleation on the glide set of the $\{111\}$ plane observed in the MD simulations may be an accurate portrayal of real SiC behavior, with the only caveat being that the transition to crack tip dislocation nucleation may occur at an even lower temperature in reality due to slip on the shuffle set of the $\{111\}$ plane. Assembling the findings of the MD simulations, analytic modeling, and DFT calculations, the transition temperature is estimated to be in the neighborhood of 300°K at ordinary strain rates, if not colder due to slip on the shuffle set.

In the end, this study suggests that the brittleness of 3C-SiC is not controlled by dislocation nucleation at temperatures above room temperature. Additionally, this work has highlighted significant challenges associated with modeling the mechanical behavior of SiC with empirical potentials, e.g. inaccurate unstable stacking fault energies and surface energies, and an artificial lattice trapping effect. Perhaps, the development of an empirical potential with longer range interatomic interactions could allow these inaccuracies to be overcome. While DFT provides a means to avoid empirical potential use altogether, its direct application to material failure studies remains hindered by its large computational cost [46,47]. A less resource intensive route would involve the use of analytic models that depend on material parameters that can be easily calculated with DFT. However, as has been shown here, the interpretation of analytic model predictions needs to be done with care, so that their limitations are clearly understood. Furthermore, the computation of the required temperature dependent material properties using DFT presents a substantial challenge, noting the importance of entropy shown here. Thus, from our perspective a silver

bullet approach for predicting the finite temperature response of a crack tip in a material like SiC does not currently exist. Therefore, an approach that consists of using multiple methods, comparing and contrasting results, as we tried to do here, remains the most promising for predicting the failure of complex materials in our opinion.

2.7 Acknowledgments

The primary support for this research was provided by Ali Sayir at AFOSR (FA9550-11-1-0273).

CHAPTER 3

KOHN-SHAM DENSITY FUNCTIONAL THEORY PREDICTION OF FRACTURE IN SILICON CARBIDE UNDER MIXED MODE LOADING

K. W. K. Leung, Z. L. Pan, and D. H. Warner

Submitted to Physical Review B

3.1 Abstract

The utility of silicon carbide (SiC) for high temperature structural application has been limited by its brittleness. To improve its ductility, it is paramount to develop a sound understanding of the mechanisms controlling crack propagation. In this manuscript, we present the first direct ab initio prediction of fracture in SiC under pure mode I and mixed mode loading, utilizing a Kohn Sham Density Functional Theory (KSDFT) framework. Our results show that in both cases, cleavage occurs on the (111) plane at a stress intensity factor (SIF) higher than the Griffith toughness. This lattice trapping effect is shown to decrease with mode mixity, due to the formation of a temporary surface bond that forms during decohesion under shear. Comparing the critical mode I SIF to the value obtained in experiments suggests that some plasticity may occur near a crack tip in SiC even at low temperatures. Ultimately, these findings provide a solid foundation upon which to study the influence of impurities on brittleness, and upon which to develop empirical potentials capable of realistically simulating fracture in SiC.

3.2 Introduction

Fracture is a prevalent failure mode in many engineered systems. However, even in the simplest cases involving very brittle materials, a comprehensive understanding of the process remains clouded. While microscopy can provide unparalleled insight, its ability to illuminate the atomic-scale events that initiate unstable crack propagation is limited due to the length and time scales involved. On the other hand, atomistic modeling can directly provide these details; however, the link between the model results and real material behavior is often unclear.

To meaningfully model the governing crack tip processes with traditional atomistic modeling techniques, a large simulation domain is needed to ensure the absence of artificial boundary effects. The large domain size limits the fidelity to which interatomic interactions can be computed, often motivating the use of empirical interatomic potentials. For brittle materials, empirical potentials often fail to accurately predict fracture due to erroneous surface energies and lattice trapping effects that result from artificially short cutoff radii.[25,48]

Higher fidelity atomistic models of crack tip behavior have recently become possible using electronic structure calculation methods, as well as concurrent multi-scale modeling methods.[49, 33, 50, 46] However, to the authors' best knowledge, electronic structure based atomistic modeling has never been utilized to study crack tip behavior in SiC, a brittle material of significant technological importance.

In prior work, we have calculated the surface energy of SiC using the Kohn Sham Density Functional Theory (KSDFT) electronic structure method, and subsequently predicted the mode I critical stress intensity factor (K_{IC}) for crack propagation using Griffith's thermodynamic fracture criterion[30] with anisotropic

elasticity. [48] The predictions were significantly below experimentally measured values. Specifically, the KSDFT Griffith prediction is $K_G = 2.0 \text{ MPa}\sqrt{\text{m}}$, while experimental measurements are $K_{IC} = 3.2 - 3.3 \text{ MPa}\sqrt{\text{m}}$. [6,7] Assuming that the KSDFT surface energy predictions are reasonably accurate and that finite temperature effects are negligible at room temperature, the discrepancy between the Griffith prediction and experiment suggests that factors beyond thermodynamics control brittle crack propagation in SiC.

To better understand the source of this discrepancy, we report here on KSDFT simulations of a crack tip under ramped loading. The simulations sought to better illuminate the mechanisms that control crack propagation in SiC, and thus, served the broader goals of (1) enabling more accurate mechanical failure predictions, (2) building a foundation upon which environmental and impurity effects can be understood, and (3) unveiling new routes for improving the toughness of this technologically promising material via impurity doping.

Despite the continuing growth of computational resources, KSDFT based atomistic prediction of crack tip response remains a challenging task. Accordingly, the primary task of this work was to conduct KSDFT atomistic simulations with limited modeling artifacts relative to real-world behavior. The manuscript begins by examining the artificial electronic effects induced by the simulation cell boundaries. Then, the artificial mechanical effects induced by the boundaries are discussed. Next, the KSDFT atomistic simulation results are presented for a sharp crack under pure mode I and mixed mode loading are presented. Under mixed mode loading, the simulations predict a critical stress intensity factor (SIF), K_{MC} , below the mode I

value, K_{IC} . The effect of mode mixity on lattice trapping is explained by examining cohesive force versus separation curves. The mode I results are compared to predictions made with Griffith's theory, empirical potential based atomistic simulation, and experimental observations.

3.3 Modeling methodology and supporting calculations

Central to the modeling effort was the use of KSDFT [51] to compute the electronic structure as a function of the position of atomic nuclei under the Born-Oppenheimer approximation.[52] The out-of-balance forces on the nuclei were computed from the electronic structure via the Hellmann–Feynman theorem.[53] The forces were then minimized with a conjugate gradient algorithm until mechanical equilibrium was obtained, a procedure that was repeated at each loading step for the crack tip simulations. Mechanical equilibrium was reached when the out-of-balance force acting on the unconstrained nuclei was less than 10 meV/Å. To reduce the computational expense, the core electrons were assumed fixed, following the ultrasoft pseudopotential approximation.[54,55] The exchange correlation functional was approximated by the generalized gradient approximation (GGA) and electron wave functions were represented with a plane wave basis set with a 240 eV energy cutoff.[56] All electronic structure computations were conducted using Vienna Ab initio Simulation Package (VASP).[57,58,59,60] Focus was directed towards the 3C-SiC crystal structure. Considering (1) the computational cost associated with this level of electronic structure fidelity, (2) the number of force computations required to reach mechanical equilibrium for each load step, and (3) our available computational

resources (approximately 200,000 hours), the crack tip simulations were limited to less than 1,000 atoms.

Because only a small nano-cluster of atoms could be modeled with KSDFT and the aim of this work was to understand SiC crack tip response in a typical bulk environment, effort was devoted to ensuring that the free surfaces of the cluster did not significantly influence the crack tip at the center of the cluster. Thus, we measured the distance over which a free surface significantly perturbs the electronic structure. The electronic effect of the free surfaces was examined using an infinite square wire of SiC with the nuclei held fixed at their bulk lattice positions. The infinite length direction of the wire corresponded to the $[\bar{1}10]$ crystallographic direction. The simulation cell was periodic in this direction and had a thickness of one lattice period. The X and Y directions of the simulation cell, corresponding to the faces of the wire, had $[11\bar{2}]$ and $[111]$ crystallographic orientation. The $[111]$ and $[\bar{1}\bar{1}\bar{1}]$ shuffle plane surfaces were carbon- and silicon-terminated, respectively, identical to the KSDFT simulations of the crack tip. The simulation cell in the X and Y directions was 55×53 Å, which corresponded to a ~ 1.5 Å vacuum layer between the periodic images of the wire surfaces. The thickness of the vacuum layer was chosen to be similar to the crack tip simulation cell discussed later. The total number of atoms in the cell was 696 and the electronic structure was computed with $1 \times 1 \times 12$ k-point integration over the Brillouin zone.

Noting that the positions of the nuclei in the wire correspond to their equilibrium positions in the bulk, nuclei sufficiently far from free surfaces are expected to have near zero net force acting on them. Nuclei closer to the surface will

experience a force from the disturbance in the electronic structure due to the free surface. In simulating the wire with a typical Methfessel-Paxton smearing energy of 0.2 eV,[61] forces greater than 20 meV/A are found on nuclei throughout the interior of the wire (Fig. 3.1). Thus, significant surface forces penetrate to beyond 26 Å from the surface. For reference, at 300 °K the expected force on a Si atom in the bulk of SiC is 1.33 eV/A, and at 0 °K the force on an unrelaxed Si surface atom is 0.82 eV/A. Considering the limited number of nuclei that can currently be modeled with KSDFT, simulating an atomic cluster of size sufficient to not have artificial surface forces (relative to the bulk) in its center is not feasible using this approach.

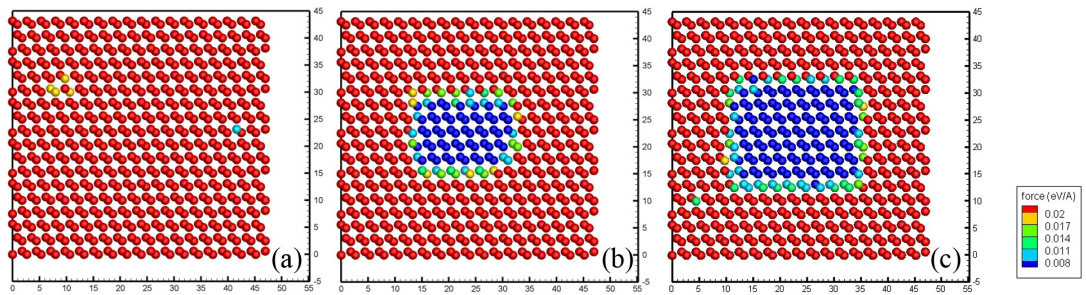


Figure 3.1: Simulation cell for pad size study. The color of the atoms represents the magnitude of the out of balance forces (eV/A) for the smearing values (a) 0.2, (b) 1.0, and (c) 1.5 eV. The unit of the axes is in Angstrom.

Three alternative approaches were considered to circumvent this challenge. The first was to terminate the SiC surfaces with hydrogen atoms, as has been previously done in the literature to compute surface energies.[62,63] However, the effect of hydrogen surface termination on the depth that surface forces penetrate is unknown. The second was to add or remove electrons from the system, i.e. dope the material. This was not observed to have an effect on the depth that surface forces penetrated, unless the doping intensity was increased to an unphysical level ($>10^{22}$

electrons per cm^3) that severely distorted other properties. The third approach, which was ultimately chosen for the crack tip simulations, was to increase the Methfessel-Paxton smearing energy used in the simulations. As the smearing energy was increased, the distance over which the free surface perturbed the electronic structure decreased dramatically (Fig. 3.1).

Because the use of high smearing energies is unphysical, the influence of the smearing energy on the material properties relevant to fracture must be considered. For the three smearing energies examined, 0.2, 1.0, and 1.5 eV, the equilibrium lattice constant, elastic constants, and the average surface energy of the C and Si terminated surfaces have been computed (Table 3.1). Details of the calculation are presented in Appendix A. Interestingly, the effect of even the highest smearing energy on the ground state material properties relevant to fracture is negligible, with the exception of the surface energy, which decreased by 17%. Given (1) the limitation on the number of atoms that can be simulated with KSDFT, (2) the desire to minimize the electronic effects resulting from the free surfaces of the atomic cluster, and (3) the desire for the KSDFT model material to resemble SiC; a 1.5 eV smearing energy was chosen for the subsequent crack tip calculations in this study. With this level of smearing, the surface forces on atoms beyond 13 Å from the free surfaces were below 8 meV/Å, and considered negligible.

Smearing (eV)	Required pad size (Å)	Lattice parameter (Å)	Surface energy of the shuffle set of the {111} plane (J/m^2)
0.2	> cell size	4.3115	4.70
1.0	17	4.3111	4.24
1.5	13	4.3088	3.91

Smearing (eV)	C_{11} (GPa)	C_{12} (GPa)	C_{44} (GPa)	Griffith's toughness (MPa \sqrt{m})
0.2	401	138	262	2.02
1.0	399	139	260	1.91
1.5	395	143	262	1.77

Table 3.1: Required pad size to meet the out-of-balance force tolerance criterion of 8meV/Å, lattice parameter, surface energy of the shuffle set {111} plane, elastic constants and Griffith's toughness for smearing parameters of 0.2, 1.0 and 1.5 eV. The surface energy reported here is the average of the C and Si terminated surfaces.

To simulate a loaded crack tip in the bulk, displacements or forces must be prescribed to the nuclei near the boundaries of the atomic cluster. To avoid artificial surface effects, the displacement or force of nuclei must be prescribed within the distance that the electronic structure is perturbed by the free surfaces. In the present case, this distance is taken to be 13 Å consistent with the preceding discussion. The region over which the displacements of the nuclei are prescribed will subsequently be referred to as the pad region. The region over which the displacements of the nuclei are not prescribed will be referred to as the core region. The goal is for the pad region to sufficiently screen the core region such that the nuclei in the core region behave as if they were in a bulk material subjected to a mechanical load applied significantly far away.

A simple approach for prescribing the applied displacement field to the pad region is to apply the anisotropic linear elastic solution for a sharp crack in an infinite medium. This one-way coupling approach is accurate in the limit of the core region being large enough to dissipate the localized effects of elastic nonlinearity and the discrete crack tip geometry. Acknowledging the limited size of the atomic cluster that

can be simulated with KSDFT, the error in applying the one-way coupling approach was examined.

The error of the one-way coupling approach was examined by comparing K_{IC} predictions against those obtained with a two-way mechanical coupling approach, i.e. the concurrent multi-scale coupled atomistic discrete dislocation (CADD) method.[47,64] In the CADD approach, the displacements are assigned to the pad atoms using the solution of an anisotropic elastic continuum boundary value problem of a large encompassing domain. The position of the outermost nuclei in the core region serve as boundary conditions to the continuum domain, and thus create a two way coupling between the core atomistic region and the surrounding continuum domain. The applied load acts over the outer boundaries of the continuum domain following the linear elastic anisotropic continuum solution for a sharp crack. In the limit that all nonlinear deformation is restricted to the core region, the pad region is of sufficient size, and the continuum region replicates the linear elastic response of the atoms, this coupling approach is error free, allowing the behavior of a crack in the bulk to be simulated with a small atomic cluster.

Computational cost prevents a direct convergence study on the effect of the core region size on K_{IC} with KSDFT. Thus, a convergence study using an empirical SiC potential[16] must serve as an analogue. The extent to which this analogue is relevant to KSDFT simulations hinges on the ability of the empirical potential to reproduce the effects of finite crack tip geometry and elastic nonlinearity observed in the KSDFT simulations.

The effect of the atomic core region size on K_{IC} was studied for the crack-crystal geometry shown in Fig. 3.2. The crack was created by displacing all atoms according to the anisotropic elastic crack field. The application of a substantial initial SIF was required to prevent crack closure. Figure 3.1 shows the results of the convergence study with both the CADD and simple one-way coupling approaches. Both approaches trend towards a converged value as the atomic core region size increases. Surprisingly, the one-way coupling approach performs very well when the atomistic box size is small, as is required here. Of course this finding is not expected to translate to cases where other crack tip mechanisms operate such as dislocation emission. Considering that the one-way coupling approach requires significantly fewer iterations to arrive at mechanical equilibrium, it is significantly less expensive computationally than the CADD approach, and therefore was chosen for the subsequent KSDFT crack tip study.

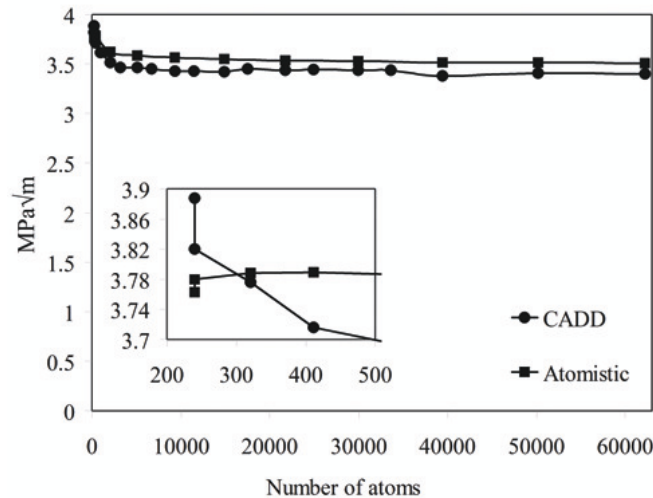


Figure 3.2: Plot of simulated K_{IC} as a function of the number of atoms in the simulation cell, i.e. atoms in both pad and core regions. Predictions are shown for the two-way coupled atomistic discrete dislocation (CADD) approach and the purely atomistic one-way coupling approach. In both cases an empirical potential was used.

The KSDFT crack tip simulations were conducted in a simulation cell with 55 Å × 53 Å in-plane dimensions, 1.5 Å vacuum layer, and one crystallographic period thick. The simulation cell consisted of 240 atoms in the core region and 456 atoms in the pad region. From the empirical potential convergence size study, we expect that this cluster size will overestimate the critical SIF by about 10% relative to an infinitely large cluster. The pad atoms were displaced following the anisotropic elastic solution for a sharp crack lying on the (111) shuffle plane with the crack front being parallel to the $\bar{1}\bar{1}0$ direction. An initial SIF was applied to prevent crack closure. The initial stress intensity factor for mode I loading was 2.24 MPa√m. For the mixed mode loading simulation ($K_{II}/K_I = 1$), an effective initial SIF of 1.92 MPa√m was used. Upon reaching equilibrium, an increment SIF of 0.016 MPa√m was applied by updating the displacement of the pad atoms. The loading process was repeated until crack propagation was observed. VMD was used for all atomistic visualization.[65]

3.4 KSDFT crack tip simulations and analysis

The critical SIF for crack growth can be identified by examining the bonds that span the (111) shuffle plane coincident with the crack plane (Fig. 3.3). Under quasi static ramped loading, the length of these bonds increases steadily until the load corresponding to the critical SIF is reached. When the critical SIF is reached, the length of a single bond increases significantly (>0.5 Å) relative to the last load step. This event can be interpreted as the rupture of the crack tip bond leading to the forward advancement of the crack by one lattice spacing. For mode I loading, the critical SIF, K_{IC} , was determined to be 2.32 MPa√m and was associated with a change

in the critical bond distance at the crack tip of 1.07 Å (Fig. 3.3(b)). Immediately prior to rupture, this critical bond was stretched to 2.76 Å, 48% longer than its unloaded equilibrium length. The predicted K_{IC} value is significantly above the prediction of Griffith's thermodynamic model, representing a significant lattice trapping effect ($R = K_{IC}/K_G = 1.32$) for mode I crack propagation. This finding is similar to what has been reported for the same orientation in silicon ($R = 1.25$).[34]

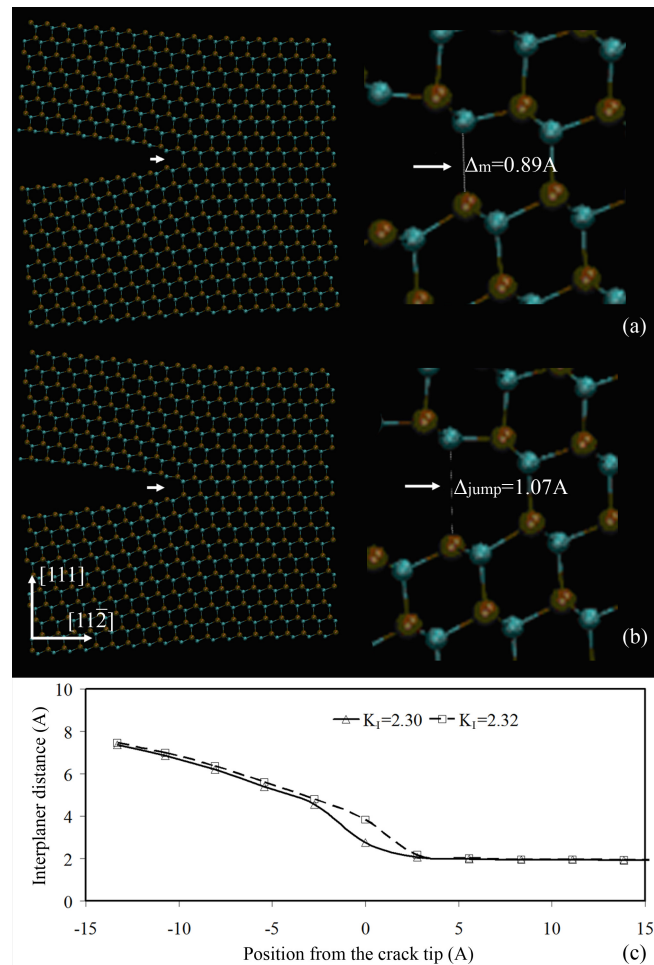


Figure 3.3: Crack growth simulation result under mode I loading: white arrow indicates the crack tip location. Si and C atoms are colored in brown and cyan respectively. (a) displays the crack tip configuration at $K_I = 2.30 \text{ MPa}\sqrt{\text{m}}$. The bond stretch for mode I loading is $\Delta_m = 0.89 \text{ \AA}$ relative to the equilibrium bond length. (b) shows the bond distance at the crack tip jumps by $\Delta_{\text{jump}} = 1.07 \text{ \AA}$ when the load is increased to $K_I = 2.32 \text{ MPa}\sqrt{\text{m}}$. (c) is a plot of the interplaner distance across the crack plane.

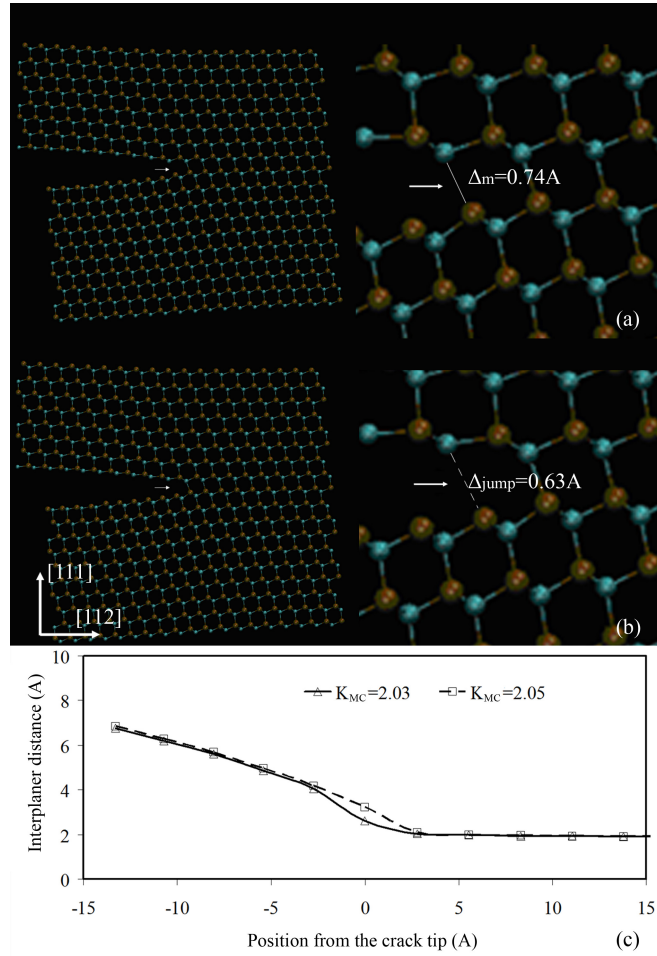


Figure 3.4: Crack growth simulation result under mixed mode loading: white arrow indicates the crack tip location. Si and C atoms are colored in brown and cyan respectively. (a) displays the crack tip configuration at $K_{MC} = 2.03 \text{ MPa}\sqrt{\text{m}}$. The bond stretch for mixed mode loading is $\Delta_m = 0.74 \text{ \AA}$ relative to the equilibrium bond length. (b) shows the bond distance at the crack tip jumps by 0.63 \AA when the load is increased to $K_{MC} = 2.05 \text{ MPa}\sqrt{\text{m}}$. (c) is a plot of the interplaner distance across the crack plane.

Figure 3.4 provides the atomistic configurations at the load step immediately before and after the application of the critical loading increment for the mixed mode loading simulation, $K_{II}/K_I = 1$. The effective critical SIF ($\sqrt{K_I^2 + K_{II}^2}$) for the mixed mode case was $K_{MC} = 2.05 \text{ MPa}\sqrt{\text{m}}$. In this case, the application of the critical load was associated with a bond distance change of 0.63 \AA at the crack tip. Immediately prior to rupture, this critical bond at the crack tip was stretched to 2.61 \AA , 40% longer

than its unloaded equilibrium length. While a significant lattice trapping barrier exists for the mixed mode loading case, $R=1.16$, it is clear that the lattice trapping barrier decreases with mode mixity.

To better understand how the result depends on the mode of the loading, we computed the cohesive force to cleave a $\{111\}$ shuffle plane as a function of displacement. Two trajectories were examined by displacing two rigid slabs consisting of 6 atomic (111) layers each, noting that size convergence studies were conducted. To mimic pure mode I loading, the slabs were displaced in the $[111]$ direction, while for $K_{II}/K_I = 1$ loading, the slabs were displaced at 65° from $[111]$, consistent with the crack tip simulation result.

When the slabs are displaced in a direction normal to the (111) plane, the cohesive force evolution qualitatively follows the well-known universal binding energy relationship,[66] despite SiC bonding not being covalent. Alternatively, when the slabs are displaced in a direction 65° from $[111]$, the cohesive force evolution displays non-monotonic behavior (Figure 3.5). This behavior is observed in both the normal and tangential components of the force, and in both cases can be attributed to the distance between originally non-bonded Si and C atoms evolving non-monotonically under $K_{II}/K_I = 1$ loading. Thus, while the primary bond between Si and C atoms at the crack tip is being ruptured, a bond between secondary Si and C atoms forms across the crack plane. For mixed mode loading, this process leads to a total cohesive force curve with lower peak forces and a longer tail (Fig. 3.5), two features that are consistent with a smaller lattice trapping effect.

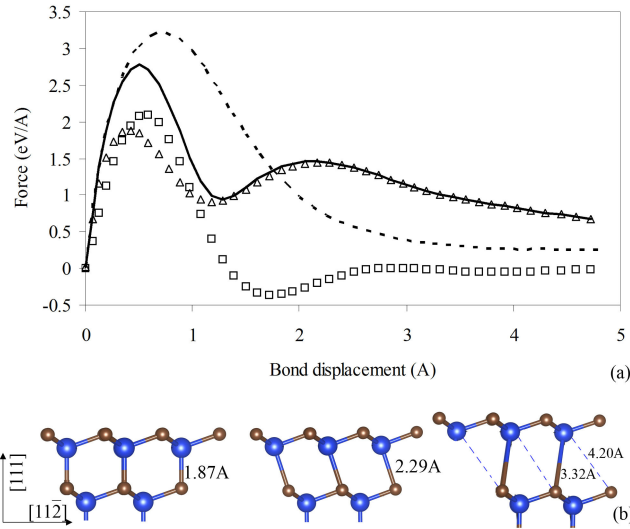


Figure 3.5: (a) plots the cohesive force as a function of bond displacement for mode I and mixed mode loading. Dotted curve represents normal cohesive force for mode I loading. Triangular symbols, square symbols and solid curve represent the normal, tangential and resultant forces for $K_{II}/K_I = 1$ respectively. (b) shows the images of the atoms that span the decohesion plane taken at different separations under the mixed mode loading trajectory. Si and C atoms are colored in red and blue respectively. A bond is drawn between Si and C atoms if the bond distance is less than 3.5Å. The left and center images show the intact primary Si-C bond before rupture. The right image displays the rupture of the primary Si-C bond (in dotted) and the new bond formed between secondary Si and C atoms across the decohesion plane.

Insight into crack tip mechanisms can be gained by comparing the K_{IC} predicted by KSDFT to room temperature experimental measurements of K_{IC} in single crystalline SiC. Acknowledging that the KSDFT simulation used (1) a 1.5 eV smearing energy, which underestimates the surface energy of the {111} shuffle set by 17 %, and (2) the finite size effect of the simulation cell overestimates K_{IC} by 10 %; we estimate a KSDFT 0 °K prediction of $K_{IC} \approx 2.3 \text{ MPa}\sqrt{\text{m}}$ if a small smearing energy and a large simulation cell size were possible. Petrovic and Roof measured K_{IC} of SiC whiskers with internal defects by loading in the [111] direction at room temperature.[7] They reported $K_{IC} = 3.23 \text{ MPa}\sqrt{\text{m}}$. Comparing with their result, the K_{IC} value predicted by KSDFT is at least $0.8 \text{ MPa}\sqrt{\text{m}}$ smaller (~28%). This suggests

that dissipative crack tip mechanisms, such as dislocation nucleation and glide, might be operative at room temperature. Despite the brittle macroscopic behavior of SiC at room temperature, this assertion is consistent with experimental observations of room temperature dislocation activity in SiC near crack surfaces,[8] under nanoindentors,[9] and in nanopillars.[67]

In a prior study,[48] we predicted $K_{IC} = 3.52 \text{ MPa}\sqrt{\text{m}}$ using the empirical potential of Devanathan et al. at 10 K.[16] As with the KSDFT simulations reported here, the value corresponded to a cleavage mechanism with no plastic slip. While the K_{IC} value matched experimental measurements, a large lattice trapping measure of $R = 2.10$ was predicted. The KSDFT results obtained here suggest that this large R value is indeed an artifact of the potential, and that our previous empirical potential predictions of K_{IC} matched experimental measurements due to offsetting errors, i.e. a low surface energy and a high lattice trapping effect. Other attempts to model fracture in SiC with empirical potentials [48,13] can also be benchmarked against the KSDFT predictions presented here.

3.5 Summary and conclusions

In summary, we have performed KSDFT calculations to study the response of a sharp crack tip in SiC under mode I and mixed mode loading. Because this study aimed to investigate crack tip response in bulk SiC, we first performed KSDFT calculations to quantify the distance required to shield the electronic perturbation of the free surface. A significant perturbation, with respect to the forces acting on the nuclei, was found to propagate beyond 26Å into the material. To address this challenge, crack tip

simulations used a Methfessel-Paxton smearing of 1.5eV to decrease the necessary shielding distance to 13Å, and subsequently allow a feasible simulation cell to be used, e.g. 696 atoms. With regard to fracture, the increased smearing energy most significantly impacted the surface energy, which was artificially decreased by 17%. Next, the mechanical effect of the simulation cell boundaries was examined, whereby a simple one-way mechanical coupling approach was found to provide a sufficient balance of computational cost versus error for our application.

KSDFT simulations of a through crack on a (111) shuffle plane with a $[\bar{1}10]$ crack front were performed to predict the critical SIF at 0 K. We obtained the critical SIF by observing a jump in the bond distance at the crack tip at the critical load. Comparing to the Griffith toughness, we found SiC to exhibit a mode I lattice trapping barrier comparable to what has been predicted previously for Si, $R = 1.32$ for SiC versus $R=1.25$ for Si.[34] We discovered that the lattice trapping barrier decreases with mixed mode loading as a result of temporary new bond formation at the crack tip during decohesion under shear loading. Even with the lattice trapping effect, the mode I predictions of K_{IC} are significantly below experimentally measured values, making crack tip dissipation mechanisms such as dislocation nucleation a plausible mechanism in SiC at low temperature.

3.6 Acknowledgments

The primary support for this research was provided by Ali Sayir at AFOSR (FA9550-11-1-0273).

3.7 Appendix A: computation methodology

For all electronic structure computation, Kohn-Sham Density Functional Theory (KSDFT) was performed with the Vienna ab initio simulation package (VASP). Core electrons were assumed fixed and approximated with ultrasoft pseudopotentials. The exchange correlation functional was approximated by generalized gradient approximating (GGA) and electron wave functions were represented with a plane wave basis set with 240 eV energy cutoff.

3.8 Appendix B: computation of cohesive force curves

The lateral X and Y directions of the simulation cell were one crystallographic period length, oriented in $[11\bar{2}]$ and $[\bar{1}10]$, respectively. The periodic Z direction consisted of 12 layers of atoms in $[111]$. The convergence of the result with respect to the number of atomic layers was tested using larger slabs. A Brillouin zone integration scheme with $8 \times 8 \times 1$ k-points was used. To compute the cohesive force curve for mode I loading, the top 6 atomic layers were rigidly displaced in $[111]$ from the bottom layers to form 2 free surfaces. Similarly for mixed mode loading with $K_{II}/K_I = 1$, the top layers were displaced at 65° from $[111]$ with respect to the bottom layers, consistent with the bond angle of the direct crack tip simulation result. All inter-atomic force calculations were performed with VASP.[16,17,18,19]

3.9 Appendix C: lattice constant, elastic constants and surface energy of the shuffle set of the $\{111\}$ plane

To examine the smearing effect on equilibrium material properties, we have calculated lattice constant, elastic constants and surface energy with smearing value of 0.2, 1.0

and 1.5 eV. A fully periodic $2 \times 2 \times 2$ unit cell was used for computing the lattice constant and elastic constants. The simulation cell was set up such that the primary directions aligned with [100], [010] and [001] directions. The Brillouin zone integration scheme consisted of $8 \times 8 \times 8$ k-points. The equilibrium lattice constant was obtained by relaxing the cell to minimum energy configuration by conjugate gradient scheme. A 0.2% uniaxial tensile strain was applied in [100] direction to calculate C_{11} and C_{12} , whereas a 0.2% shear strain was applied to calculate C_{44} .

The fracture mechanisms of a brittle crack tip are dictated by the surface energy of the fracture plane. To quantify the effect of smearing on surface energy, we have calculated the surface energy of the {111} shuffle plane. An infinite film with {111} plane aligning with the top and bottom free surface was used to calculate the surface energy. Full periodic boundary condition was applied with X and Y axis corresponding to $[11\bar{2}]$ and $[\bar{1}10]$ direction respectively. The z direction consisted of 2-6 SiC {111} layers and a 17.5 Å thick vacuum layer, resulting in two {111} shuffle plane surfaces. Brillouin zone integration with $8 \times 8 \times 1$ kpoints and Methfessel-Paxton smearing of 0.2, 1.0 and 1.5 eV were employed. All parameters including the simulation cell size and vacuum thickness were tested to ensure energy convergence. The atomic positions of the top three Si-C {111} layers were relaxed to the minimum energy configuration by conjugate gradient method for the relaxed surface energy. The total energy of the system containing n Si-C {111} layers can be expressed from the equation, $E = E_1 n + \gamma A$, where E and E_1 represent the total energy of the system and the energy per Si-C {111} layer respectively; γ is the surface energy and A is the

surface area. The surface energy then can be obtained from a least square fit from the plot of total energy versus number of Si-C layers. The relaxed surface energy of the {111} shuffle plane and the required pad thickness associated with the smearing values are presented in Table 1 of the text. The calculation shows that a smearing value of 1.5 eV provides a good balance between the pad thickness and the deviation of the fracture surface energy.

3.10 Appendix D: surface relaxation of the crack plane

The positions of atoms in the pad region near the free surfaces of the crack have to be prescribed consistent with their surface relaxation to avoid artificial forces in the crack tip simulation cell. We studied the surface relaxation of the {111} shuffle plane for both Si- and C-terminated surfaces. The simulation cell is the same as that for the computation of the relaxed surface energy. The top 6 layers of atoms were relaxed to minimum energy positions. The {111} shuffle surface of SiC undergoes significant surface relaxation according the calculation. The atomic positions of the 6 Si-C surface layers of the crack free surfaces were initialized according to the relaxed positions displayed in Fig. 3.6.

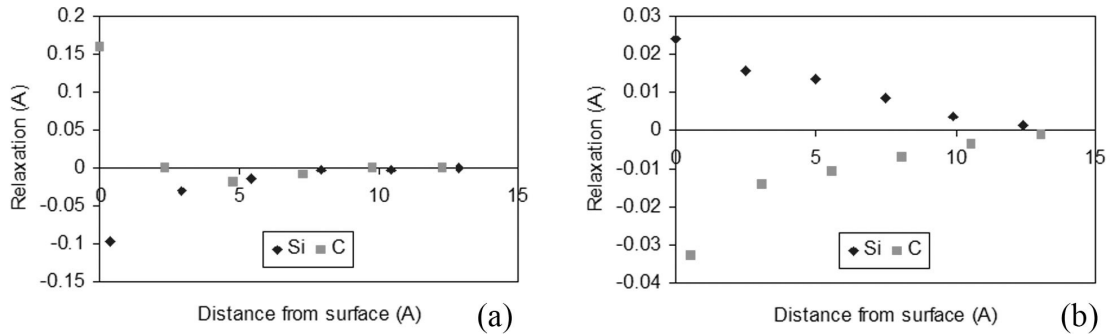


Figure 3.6: Surface relaxation of (a) C-terminated surface and (b) Si-terminated surface for the shuffle set of the {111} plane. Negative values correspond to outward atomic relaxation.

CHAPTER 4

ATOMISTIC PREDICTION OF IMPURITY EFFECTS ON THE INTRINSIC BRITTLENESS OF SILICON CARBIDE

By K. W. K. Leung and D. H. Warner

4.1 Abstract

The impurity effects on the fracture toughness of silicon carbide (SiC) single crystal have remained elusive due to the complex mechanisms at a SiC crack tip. To better illuminate the impurity effects on the key mechanisms, we used high fidelity ab-initio Kohn Sham Density Functional Theory (KSDFT) calculation to examine the decohesion and slip resistance of the $\{1\ 1\ 1\}$ plane in the presence of impurity atoms. Because of the high computation cost of direct crack tip simulation using electronic structure calculation, we modified a SiC empirical potential to match the KSDFT calculations by strategically shielding critical bonds at the crack tip. The strategic bond shielding approach was implemented in a molecular dynamics framework to predict the critical mode I stress intensity factor (K_{IC}) for crack propagation. Nitrogen, phosphorus, silicon and hydrogen impurities always embrittle SiC as these impurities enhance surface decohesion over dislocation nucleation. In contrast, for aluminum, boron and carbon impurities, K_{IC} exhibits a non-monotonic effect, i.e. it first increases then decreases as a function of impurity concentration. This is attributed to an increase in dislocation kink nucleation at low concentration and a transition from dislocation kink nucleation to kink propagation at high concentration. Our studies also serve broader goals of understanding impurity and environmental effects via physics based

model and unveiling possible routes to improve fracture toughness of complex materials.

4.2 Introduction

Silicon carbide (SiC) is a promising material for enabling next generation aerospace and semiconductor technologies in harsh environments [1,2,3,4,5]. It has a high melting temperature, thermal conductivity, stiffness, hardness, electron mobility and a large band gap. SiC resists corrosion and creep, while having a low thermal expansion coefficient and low density. However, the utilization of SiC's impressive properties is often hindered by its susceptibility to fracture. SiC exhibits brittle fracture at low temperature, with experimental fracture toughness of $K_{IC} \approx 3.2 \text{ MPa}\sqrt{\text{m}}$ for single crystalline SiC [6,7]. This value is higher than the K_{IC} predicted from the surface energy of the preferred cleavage plane, $K_{IC} = 2.0 \text{ MPa}\sqrt{\text{m}}$, computed with Kohn Sham Density Functional Theory (KSDFT) calculation in our prior studies [48]. This indicates that fracture toughness is a consequence of not only the cohesive energy, but also crack tip plasticity by energy dissipative mechanisms such as dislocation nucleation and glide, even at room temperature.

SiC is often used in close proximity to a wide range of impurity elements. To protect it from degrading in harsh environments, environmental barrier coatings consisting of exotic metals are often used, such as barium strontium aluminum silicate [68]. To utilize its electronic properties, it is often doped with boron, nitrogen and phosphorus [69]. The direct effect of such impurity elements on its mechanical response has not been established, and thus these potentially important chemo-

mechanical effects are absent from materials design and prognosis. This challenge has motivated our prior and present studies to (1) illuminate key crack tip mechanisms by studying a SiC crack tip, (2) examine the impurity effects on these mechanisms that ultimately control the macroscopic fracture behaviors and (3) possibly unveil means for improving its fracture toughness by doping.

Although the effect of impurities on fracture toughness can be directly examined with experiments, simulations offer a less expensive and more controlled way to explore this problem. Furthermore, atomistic simulations can provide insight into atomic scale mechanisms such as bond breaking and dislocation nucleation, and the impurity effects on those mechanisms, which ultimately control the intrinsic toughness of a material. While direct simulation of the crack tip with KSDFT calculation is possible, only a few simulations can be conducted due to its high computation cost. With the development of multi-scale simulation method and the growth of computing resources, concurrent multi-scale coupled atomistic discrete dislocation (CADD) method was developed [46] to directly investigate an aluminum crack tip in the presence of oxygen and hydrogen at the surface of the crack tip [47]. While this method was able to predict the stress intensity factor for dislocation nucleation in the presence of a single impurity atom, only a few crack tip configurations with limited impurity atom can be examined. As small variations in impurity positions can lead to significantly different crack tip response, it is impossible to generate a generalized understanding with this approach.

DFT calculations have also been utilized to compute input parameters to continuum models that are used to predict crack tip trends with the theory of fracture

mechanics and dislocation. For example, [70] studied the effects of dopants on the generalized stacking fault energies and identified doping elements that improved the ductility of Mg. A new dis-embrittlement parameter $D = \gamma_s/\gamma_{us}$ was used by Waghmare et al. to assess if an alloying atom enhanced the ductility of MoSi₂, where γ_s is the surface energy of the potential cleavage plane and γ_{us} is the unstable stacking fault energy of the potential slip plane [71]. Based on the mechanical properties computed with first principles calculations, [72] used the Rice-Thomson (R-T) parameter $\mu b/\gamma_s$ to evaluate the impurity effects on the ductility of Mo alloy, where μ and b are the shear modulus and Burgers vector respectively. [73] utilized DFT calculations to compute the fracture energy of metals as a function of H coverage on the cleavage surface and attributed hydrogen embrittlement to cohesion-reduction mechanism. While these first principles calculations provide insight into impurity effects on slip and decohesion, they are first order approaches that can not capture complex mechanisms such as lattice trapping effect, dislocation kink propagation and dislocation core reconstruction.

Empirical potential based simulations are often used to explore the large parameter space for crack tip studies because of a lower computation cost. However, empirical potentials for covalent materials often fail to capture the fracture behavior even qualitatively. Particularly, for pure SiC, empirical potential exhibit large lattice trapping effect and cannot predict the crack tip response accurately. Hence, we propose a combined approach, utilizing the strengths of KSDFT and empirical potentials based simulations approaches to understand the real SiC behavior.

In this manuscript, we first reported on our KSDFT calculations of the impurity effects on decohesion energy for $\{1\ 1\ 1\}$ shuffle plane and slip energy for $\{1\ 1\ 1\}$ shuffle and glide planes as these planes were identified as the preferred cleavage and slip planes for SiC in our prior studies. Our results revealed that the impurity position relative to the decohesion and slip plane can have different influence on the decohesion and slip resistance. To connect these findings with SiC crack tip response, the impurity effects were incorporated into a novel and non-transferable empirical-based strategic bond shielding approximation (SBSA) approach. This approach was implemented in a molecular dynamics (MD) framework with modified empirical potential to match the KSDFT calculation results by strategically shielding critical bonds on the potential decohesion and slip planes. After matching the fracture response of pure SiC with prior KSDFT results using SBSA approach, we simulated impurity effects on the critical stress intensity factor (K_{IC}) under mode I loading. Our study focused on SiC crack tip response at low temperature because SiC has lower fracture toughness at low temperature which is likely to control the design of structural components. Our results revealed that K_{IC} depends on the type and concentration of impurity near the crack front. The crack tip mechanisms are a result of two competitions of mechanisms: the competition between cleavage and dislocation nucleation; and the competition between dislocation kink nucleation and propagation. Acknowledging the inaccuracies of the empirical potential, we examined our results by comparing to KSDFT calculations and concluded the impurity effects on real-world SiC crack tip behavior.

4.3 DFT Simulation Methodology

Given a sufficient separation of length scales, $K_I > K_{IC}$ is an accurate and general criterion for mode I crack growth. Considering Griffith's widely used analytic model [30], crack growth occurs when it is thermodynamically favorable, i.e. $G > 2\gamma_s$, where G is the strain energy release rate. γ_s represents the surface energy of the cleavage plane and its value can provide an indicator for the resistance to decohesion. Similarly, Rice [23] proposed that dislocation nucleates from a crack tip when $G > \alpha\gamma_{us}$, where α depends on the geometry of the slip direction relative to the crack. γ_{us} is the unstable stacking fault energy and represents the resistance to slip of a crystal. We quantified the impurity effects on decohesion and slip utilizing a similar concept. We started by examining the change in decohesion resistance ($\Delta\Gamma_d$) and the change in slip resistance ($\Delta\Gamma_s$) in the presence of impurities using KSDFT approach. The simulation cell was fully periodic in all directions, with its lateral directions equaled 3 and 2 crystallographic period length in $[1 \ -1 \ 0]$ and $[1 \ 1 \ -2]$, respectively. The vertical direction consisted of 12 layers of atoms in $[1 \ 1 \ 1]$. Six substitution impurities were examined, by substituting silicon (Si) or carbon (C) sites with aluminum (Al), boron (B), C, nitrogen (N), phosphorus (P) and Si atoms on the 3 $\{1 \ 1 \ 1\}$ layers closest to the decohesion or slip surfaces (Figure 4.1 and 4.2). A single Si atom on the $\{1 \ 1 \ 1\}$ plane was replaced by Al, P and C atom. A single C atom on the $\{1 \ 1 \ 1\}$ plane was replaced by B, N and Si atom. The substitution sites were determined such that the binding energy of the impurity is the lowest in the crystal relative to other possible sites according to first principles studies [74,75,76]. H atoms were placed at the interstitial sites with the smallest binding energy among other sites. The substitution and

interstitial sites are shown in Figure 4.1 and 4.2 for calculating $\Delta\Gamma_d$ and $\Delta\Gamma_s$ of the shuffle set and glide set of the $\{1\ 1\ 1\}$ plane.

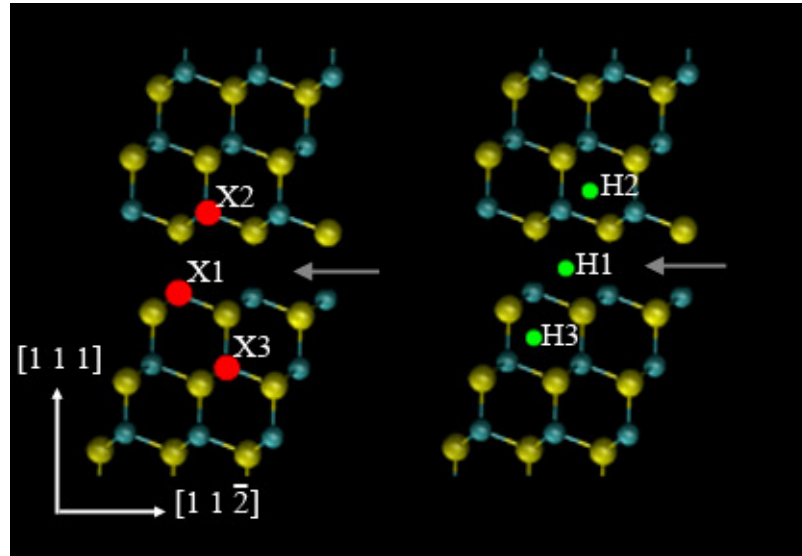


Figure 4.1: Substitution and interstitial impurity sites for $\Delta\Gamma_d$ and $\Delta\Gamma_s$ of the shuffle set of the $\{1\ 1\ 1\}$ plane. X1, X2 and X3 represent substitution impurity on plane 1, 2 and 3, respectively. H1, H2 and H3 represent interstitial impurity on plane 1, 2 and 3, respectively. The grey arrow indicates the location of the shuffle plane.

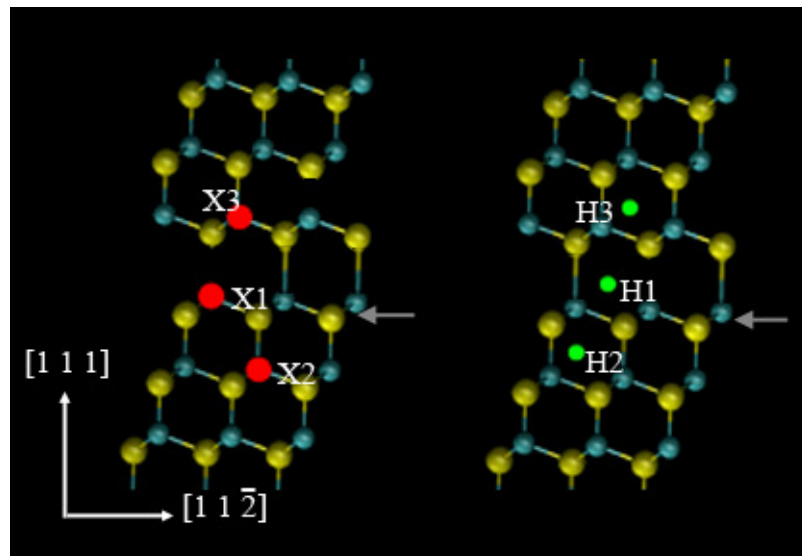


Figure 4.2: Substitution and interstitial impurity sites for $\Delta\Gamma_s$ of the glide set of the $\{1\ 1\ 1\}$ plane. X1, X2 and X3 represent substitution impurity on plane 1, 2 and 3,

respectively. H1, H2 and H3 represent interstitial impurity on plane 1, 2 and 3, respectively. The grey arrow indicates the location of the glide plane.

All KSDFT calculations were performed with the Vienna Ab-initio Simulation Package (VASP) [53]. Core electrons were assumed to be fixed using ultrasoft pseudopotential model [54,55]. The exchange and correlation of electrons were approximated with generalized gradient approximation (GGA) [77]. The cell was discretized with a plane-wave basis set having cutoff energy of 240 eV. Brillouin zone integration was performed with a $8 \times 8 \times 1$ k-point mesh. The energy cutoff and the number of k-points were tested to ensure energy convergence.

As the shuffle set of the $\{1\ 1\ 1\}$ plane was identified as the preferred cleavage plane for SiC in our prior studies [48], we began with the examination of $\Delta\Gamma_d$ of this plane. In the simulation, the top 6 layers were separated from the lower layers incrementally to impose decohesion on the shuffle set of the $\{1\ 1\ 1\}$ plane. As a result, a vacuum layer was formed between the top and bottom layers. The change in decohesion resistance with impurity on plane i is given by, $\Delta\Gamma_d = \Gamma_{di} - \Gamma_d$, where $\Gamma_{di} = E_{di} - E_{oi}$ and $\Gamma_d = E_d - E_o$. E_{di} and E_{oi} are the total energy of the system with impurity on plane i , with and without decohesion respectively. E_d and E_o are the total energy without impurity, with and without decohesion respectively.

Although the plasticity of SiC is still under research, it is often attributed to slip occurs on the shuffle set of the $\{1\ 1\ 1\}$ plane in $\langle 1\ 1\ 0 \rangle$ with full dislocation at room temperature [9] and the glide set of the $\{1\ 1\ 1\}$ plane in $\langle 1\ 1\ 2 \rangle$ with leading and trailing partial dislocation at higher temperature [10]. Since the presence of impurity may favor slip on a different system, another plausible slip system on the

shuffle set of the $\{1\ 1\ 1\}$ plane in $\langle 1\ 1\ 2 \rangle$ was also considered. This slip system consists of two distinct directions to form full dislocation, first shearing along $[1\ 1\ -2]$ and then along $[2\ -1\ -1]$. To compute the change in slip resistance with impurities, the top 6 layers were shifted incrementally in the Burgers vector direction with respect to the bottom layers. The slip resistance is defined at a location on the slip path where the stacking fault energy reaches a maximum. Note that this is the unstable stacking fault energy multiplied by the slip area. The change in slip resistance with impurity on plane i is defined by $\Delta\Gamma_s = \Gamma_{si} - \Gamma_s$, where $\Gamma_{si} = E_{si} - E_{oi}$ and $\Gamma_s = E_s - E_o$. E_{si} and E_{oi} are the total energy of the system with impurity on plane i , with and without slip respectively. E_s and E_o are the total energy without impurity, with and without slip respectively.

4.4 DFT calculation results

$\Delta\Gamma_d$ for the shuffle set of the $\{1\ 1\ 1\}$ plane are shown in figure 4.3. Of all planes considered, impurities located directly on the decohesion plane (plane 1) exhibit the largest effect. All impurities decrease the decohesion resistance by 0.08 – 1.67 eV except when Al substitutes Si on plane 2 and when Si substitutes C on plane 1 and 3. In the first case, $\Delta\Gamma_s$ is +0.01 eV. The substitution of C by Si cases are the outliers, where $\Delta\Gamma_d$ is smaller than -2.5 eV when C is substituted by Si on plane 1 and 3. Relative to other cases, the large atomic size difference between Si and C creates strain misfit, resulting in a large amount of surface reconstruction that reduces the decohesion resistance of the shuffle plane significantly. Overall, it is reasonable to

expect that the presence of impurities near the cleavage plane reduces the decohesion resistance at a crack tip.

While there are no published experimental results on the impurity effects on decohesion energies of SiC for comparison, our results are consistent with simulation predictions for other materials. Hong and Chou [78] studied the effect of hydrogen on surface energy of diamond and silicon and found that as the number of hydrogen atom increases, the surface energies for (1 0 0), (1 1 1) and (1 1 0) plane decrease. Waghmare [71] computed the surface energy of MoSi₂ when Si is replaced by other elements using KSDFT calculations and reported all elements decrease surface energy.

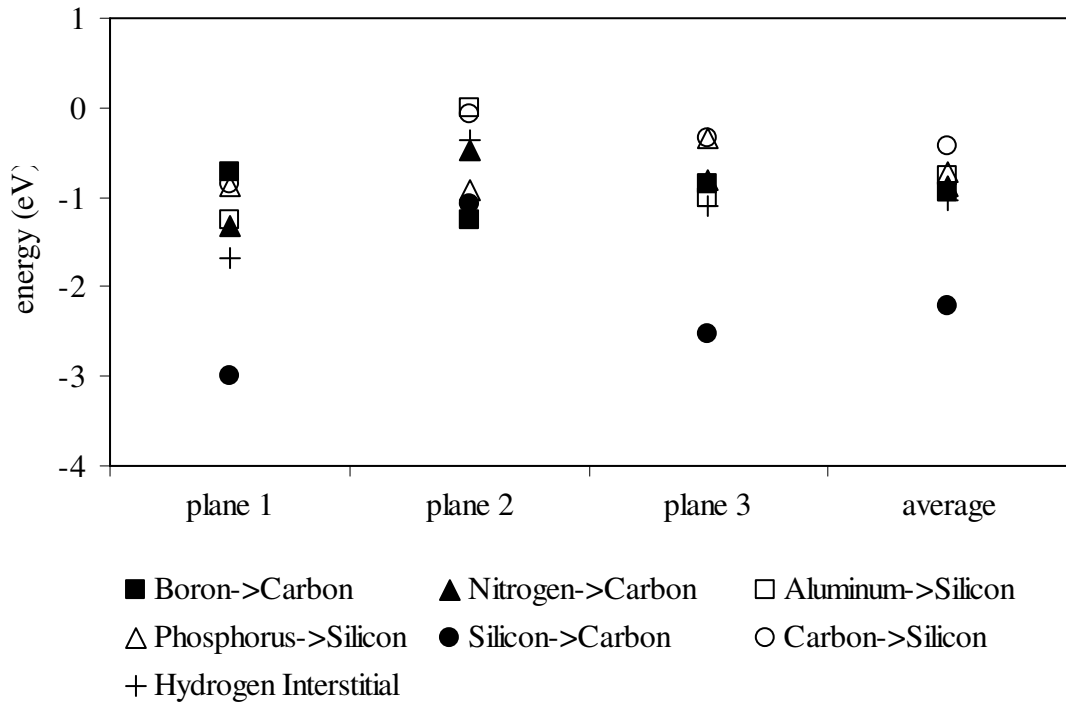


Figure 4.3: $\Delta\Gamma_d$ for the shuffle set of the {1 1 1} plane with impurity on 3 sites. Plane 1, 2 and 3 correspond to the impurity sites illustrated in figure 1. The average $\Delta\Gamma_d$ of the three planes are also presented.

$\Delta\Gamma_s$ for the glide set of the $\{1\ 1\ 1\}$ plane with Burgers vector in $[1\ 1\ 2]$ are shown in figure 4.4, with both leading and trailing partial dislocation on the glide set having the same $\Delta\Gamma_s$. Most impurities decrease the slip resistance except for P and C on plane 2 and N and H on plane 3. In general, p type impurities such as Al and B have the largest effect and n type impurities such as N and P have the least effect on the decrease of slip resistance, suggesting that dislocation slip on the glide plane is sensitive to electronic structure.

$\Delta\Gamma_s$ for nucleating full dislocation in $[1\ 1\ 0]$ on the shuffle set of $\{1\ 1\ 1\}$ plane are shown in figure 4.5. All impurities decrease the slip resistance except when C substituted Si on plane 1 and 2. $\Delta\Gamma_s$ for nucleating full dislocation on the shuffle set of $\{1\ 1\ 1\}$ with slip path in $[1\ 1\ 2]$ are shown in figure 4.6. For the shuffle set, the most significant decrease in slip resistance occurs when C is replaced by Si and the most significant increase occurs when Si is replaced by C, suggesting that dislocation slip on the shuffle set is sensitive to misfit strain.

In summary, the changes in slip resistance are the most significant when the impurities locate nearest to the slip plane at the crack tip. Considering the presence of impurities can either increase or reduce the slip resistance on the glide and the shuffle set depending on impurity site, it cannot be concluded if slip nucleation is more favorable on the glide set or on the shuffle set in the presence of impurities.

To authors' best knowledge, the impurity effects on the slip resistance for SiC are unknown. Although the slip in covalent material involves complex processes such as the reconstruction of the dislocation core, a lower slip resistance is often correlated with a lower activation energy for dislocation glide and a higher dislocation

mobility. Our study is in agreement with the experimental results in Si [79,80], where impurities decrease the activation energy of dislocation glide and increase dislocation velocity. Our results can also be compared to an ab-initio calculation of activation energy for dislocation glide in SiC using local density functional cluster method [81], which predicted n type impurity increases the mobility of C partials and p type impurity increases the mobility of Si partials on the glide set.

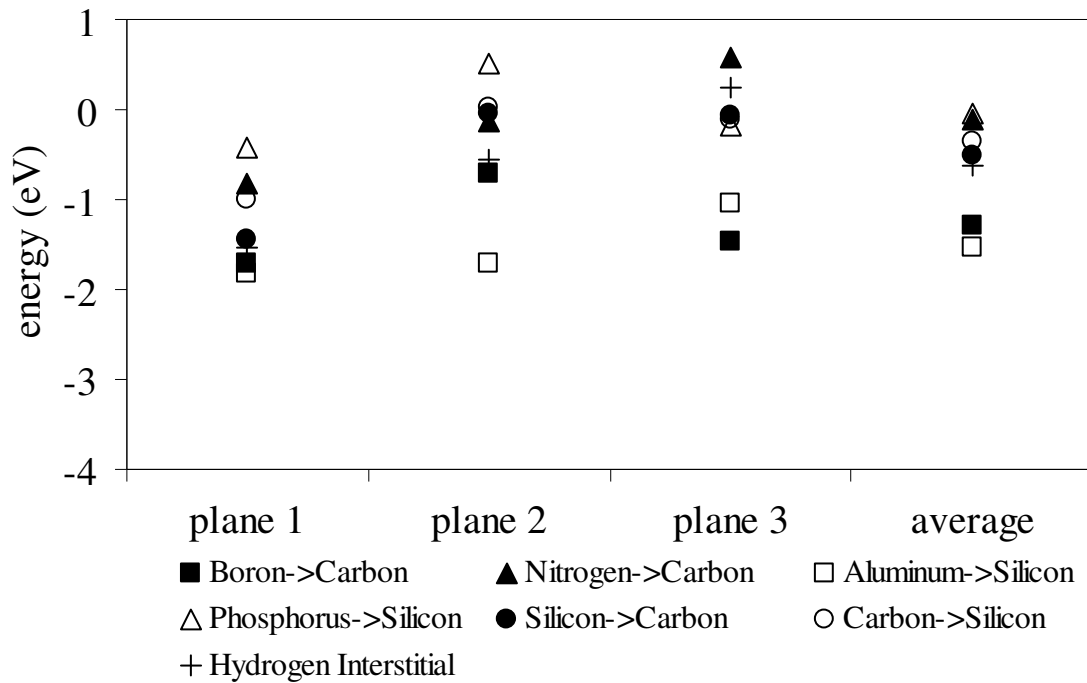


Figure 4.4: $\Delta\Gamma_s$ for the glide set of the $\{1\ 1\ 1\}$ plane in $[1\ 1\ 2]$ with impurity on 3 sites. Plane 1, 2 and 3 correspond to the impurity sites illustrated in figure 2. The average $\Delta\Gamma_s$ of the three planes are also presented.

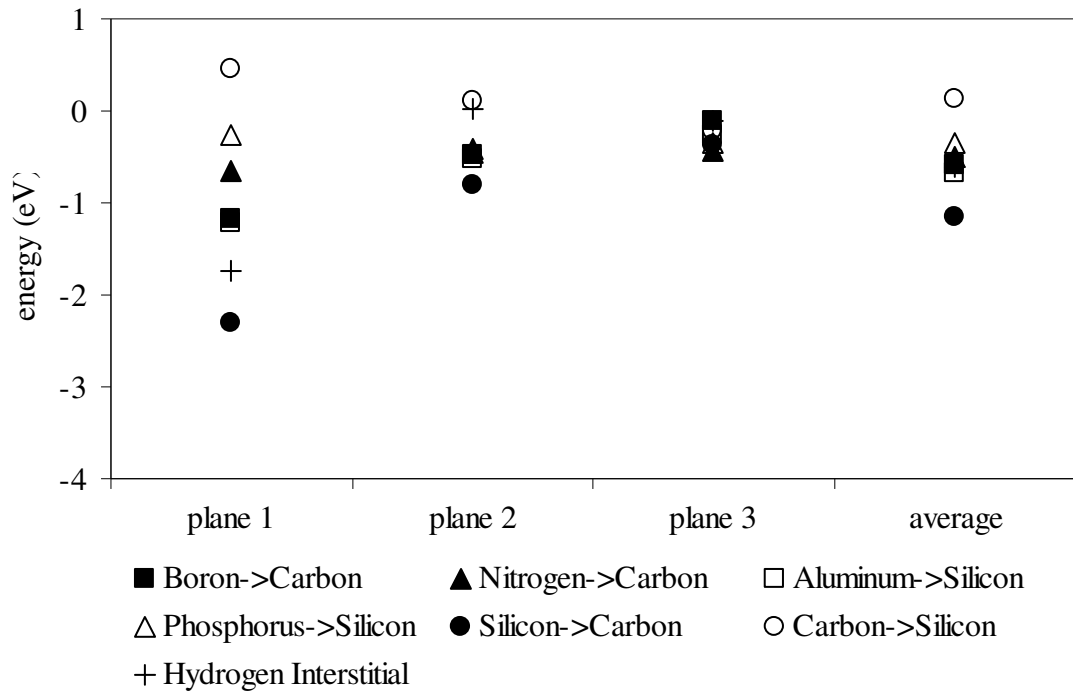


Figure 4.5: $\Delta\Gamma_s$ for the shuffle set of the $\{1\ 1\ 1\}$ plane in $[1\ -1\ 0]$ with impurity on 3 sites. Plane 1, 2 and 3 correspond to the impurity sites illustrated in figure 1. The average $\Delta\Gamma_s$ of the three planes are also presented.

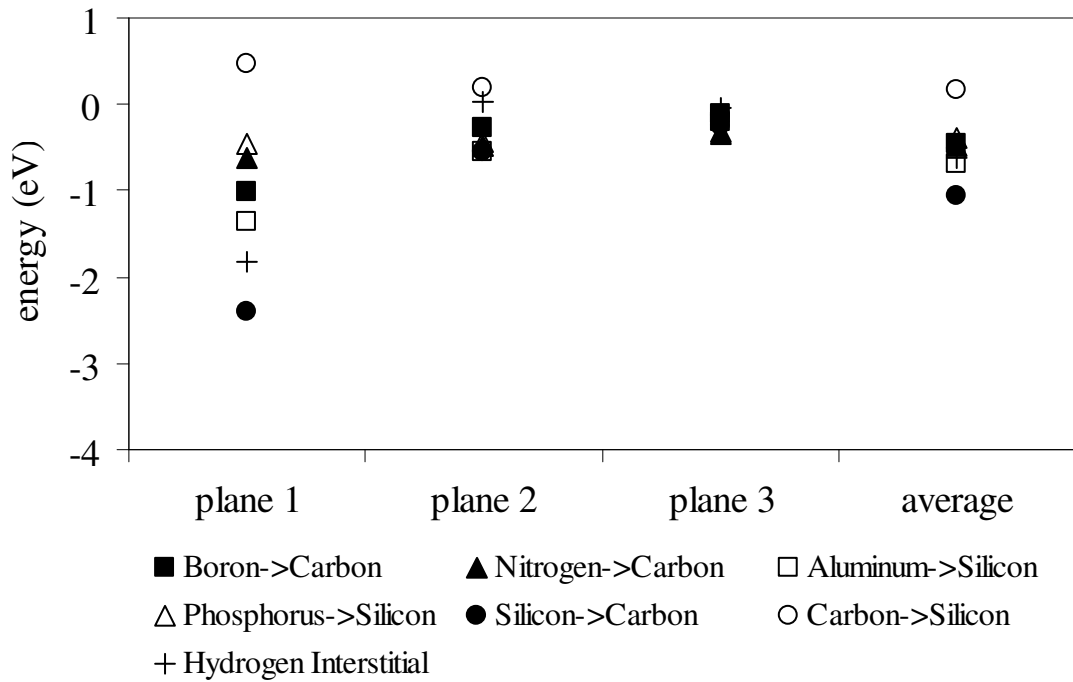


Figure 4.6: $\Delta\Gamma_s$ for the shuffle set of the $\{1\ 1\ 1\}$ plane in $[1\ 1\ -2]$ with impurity on 3 sites. Plane 1, 2 and 3 correspond to the impurity sites illustrated in figure 1. The average $\Delta\Gamma_s$ of the three planes are also presented.

4.5 MD simulation setup

While higher fidelity DFT calculations shed light on the impurity effects on decohesion and slip resistance, due to the computational expense, it remains impractical to simulate the change in K_{IC} as a function of impurity concentration directly. First, a large spatial domain is required to shield the artificial surface effects from the crack tip. Second, at atomic scale, small variations in the crystal structure lead to significant different material response. The configuration space is large because of the statistical nature of impurity effects on crack growth. Thus, empirical potential based MD simulations must be used to study the change in K_{IC} as a function of impurity type and concentration.

The atomistic simulations were performed in LAMMPS package [21] with Devenathan et al. potential for SiC [16]. The simulation box size was 120 x 150 x 19 Å (X x Y x Z) oriented in $[1\ 1\ -2]$, $[1\ 1\ 1]$ and $[1\ -1\ 0]$ respectively. X direction was traction free and Z direction was periodic to represent a plane strain condition. Tensile stress was applied by enforcing an average displacement of the atoms along the Y boundaries. An initial 50 Å crack was created by shielding interaction between atoms above and below the shuffle set of a $(1\ 1\ 1)$ plane. The energy of the system was minimized using conjugate gradient scheme for each load increment. The doped samples were created by assigning impurity atoms randomly in the sample given an impurity concentration. To capture the statistical nature of the problem, multiple simulations were performed for an impurity concentration value. The effect of

specimen size including in-plane dimensions and thickness was investigated to ensure the convergence of the minimum value of K_{IC} , as the toughness of SiC at realistic scale is likely to be controlled by the K_{IC} when the impurities are at the most detrimental positions. Because the crack tip response can vary significantly for different impurity locations, the K_{IC} convergence study required to sample all possible impurity positions along the crack thickness.

According to our prior studies, the empirical potential employed in our simulations underestimates the surface energy for the shuffle set of the $\{1\ 1\ 1\}$ plane and overestimates the lattice trapping effect. Thus, we used a strategic bond shielding approximation (SBSA) approach to match the empirical simulation result with the KSDFT result for cleavage of pure SiC by choosing the critical decohesion resistance in energy unit (Γ_d^c). The forces between bonds around the crack tip are shielded if the bonds experience di-atomic energy greater than Γ_d^c . With SBSA approach, we were able to match the K_{IC} predicted by DFT simulation for pure SiC. Note that we can only match the cleavage response with the SBSA approach because cleavage always occurs before dislocation nucleation in prior DFT study. The ability to capture realistic slip response of pure SiC relies on the unstable stacking fault energies of the empirical potentials, which were found to be overestimated except for the glide set. Thus, it is expected the empirical potential based simulation with SBSA approach will underpredict the occurrence of slip on the shuffle set relative to real-world SiC behavior.

To mimic the impurity effects on decohesion and slip, SBSA was employed to modify the interactions between the crack tip atoms. It implemented the following

procedures: (1) The energy of the system was minimized using conjugate gradient scheme to relax atoms to their equilibrium positions; (2) for bonds around the crack tip, search for impurity atoms adjacent to the bond and determine $\Delta\Gamma_d$ based on impurity positions relative to the bond. Any di-atomic bonds that were susceptible to rupture with di-atomic energy greater than the effective decohesion resistance (Γ_d^e) were stored in a decohesion shielding list. Γ_d^e is defined as the difference between Γ_d^c and $\Delta\Gamma_d$ to match the DFT results; (3) slip events were checked in a similar way as decohesion events. Any di-atomic bonds that were susceptible to slip with di-atomic energy greater than the effective slip resistance (Γ_s^e) were store in a slip shielding list. Γ_s^e is defined as the difference between the critical slip resistance (Γ_s^c) and $\Delta\Gamma_s$ to match the DFT results. Γ_s^c is the energy between the slipped atoms in the unstable stacking fault configuration; (4) if both shielding lists were not empty, the atoms of the critical bonds were completely shielded by cancelling the forces from each other. Then, procedures (1) to (3) were repeated until no new shielding event was detected; (5) after equilibrium was reached, the load was incremented by displacing the atoms along the Y boundaries. As the shielding list was re-initialized every load step, the shielded bonds from the previous load step were only shielded only if the shielding criteria were fulfilled.

4.6 MD simulation results

The normalized K_{ICs} , by K_{IC} of pure SiC, are plotted as a function of impurity concentration for different impurities in figure 4.7-13(a). From these plots, two major trends were observed. First, as impurity concentration increased, the average K_{IC}

values decreased. This trend was consistent for all impurity elements studied. K_{IC} values dropped by approximately 50% at a concentration of 8×10^{21} atoms/cm³. Second, samples doped with Al, B or C at concentration $< 2 \times 10^{21}$ atoms/cm³ had higher average K_{IC} values relative to pure SiC. To illustrate this point, the normalized K_{IC} distributions are plotted in figure 4.7-13(b) in 2 groups, impurity concentration $< 2 \times 10^{21}$ and $> 2 \times 10^{21}$ atoms/cm³.

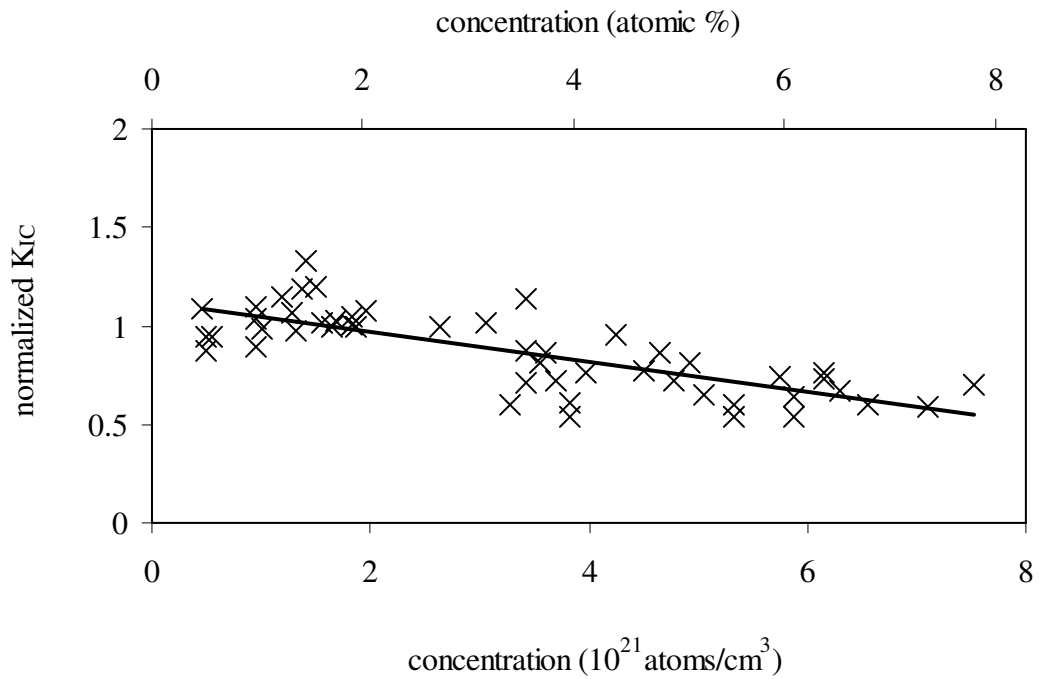


Figure 4.7(a): Normalized K_{IC} as a function of B impurity concentration.

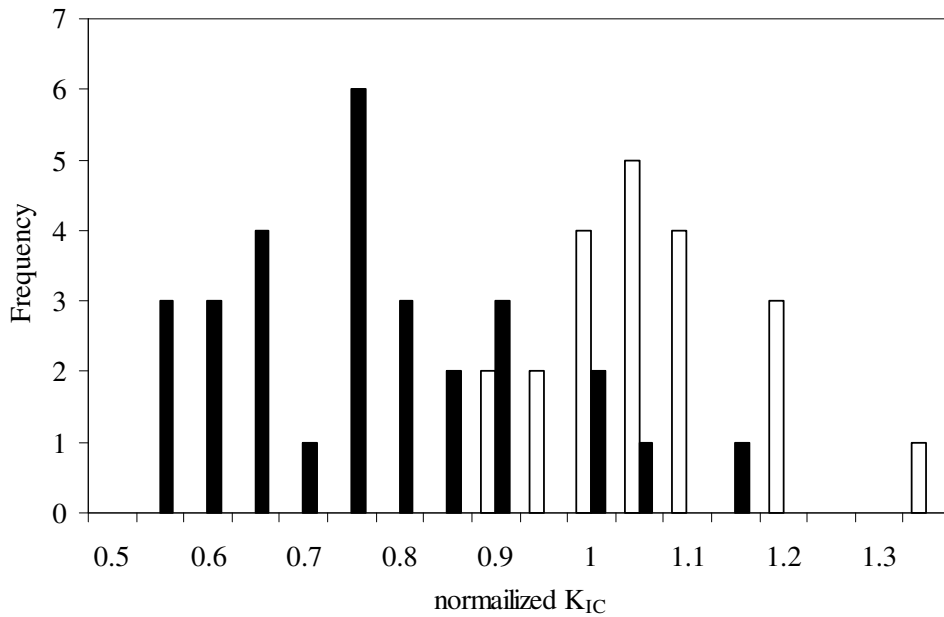


Figure 4.7(b): Normalized K_{IC} frequency plot for B impurity. Filled columns represent impurity concentration $< 2 \times 10^{21}$ atoms/cm³ and unfilled columns represent impurity concentration $> 2 \times 10^{21}$ atoms/cm³.

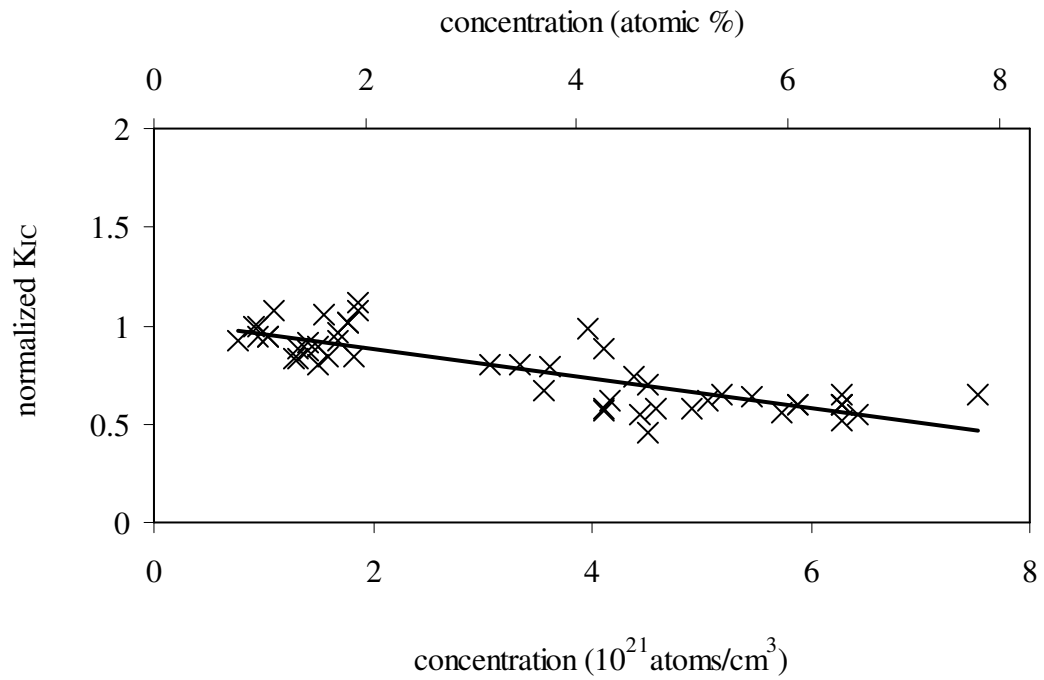


Figure 4.8(a): Normalized K_{IC} plotted as a function of N impurity concentration.

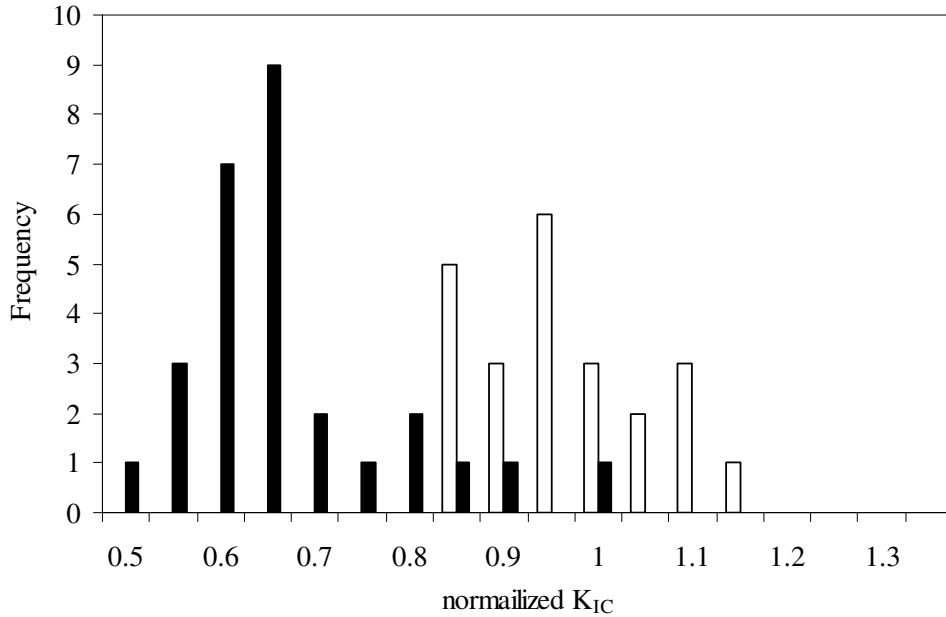


Figure 4.8(b): Normalized K_{IC} frequency plot for N impurity. Filled columns represent impurity concentration $< 2 \times 10^{21}$ atoms/cm³ and unfilled columns represent impurity concentration $> 2 \times 10^{21}$ atoms/cm³.

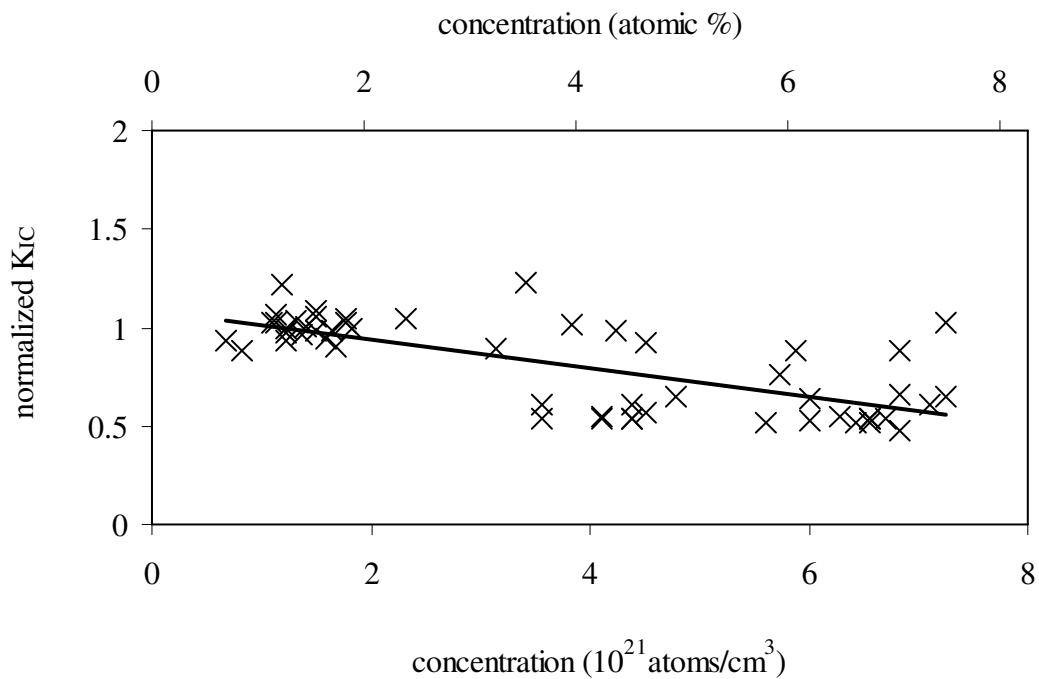


Figure 4.9(a): Normalized K_{IC} plotted as a function of Al impurity concentration.

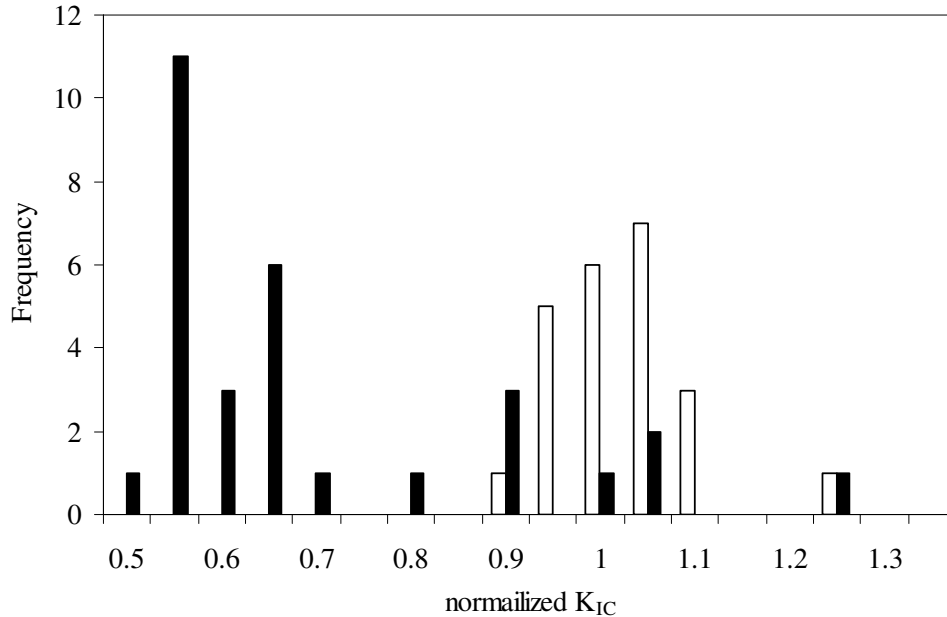


Figure 4.9(b): Normalized K_{IC} frequency plot for Al impurity. Filled columns represent impurity concentration < 2 × 10²¹ atoms/cm³ and unfilled columns represent impurity concentration > 2 × 10²¹ atoms/cm³.

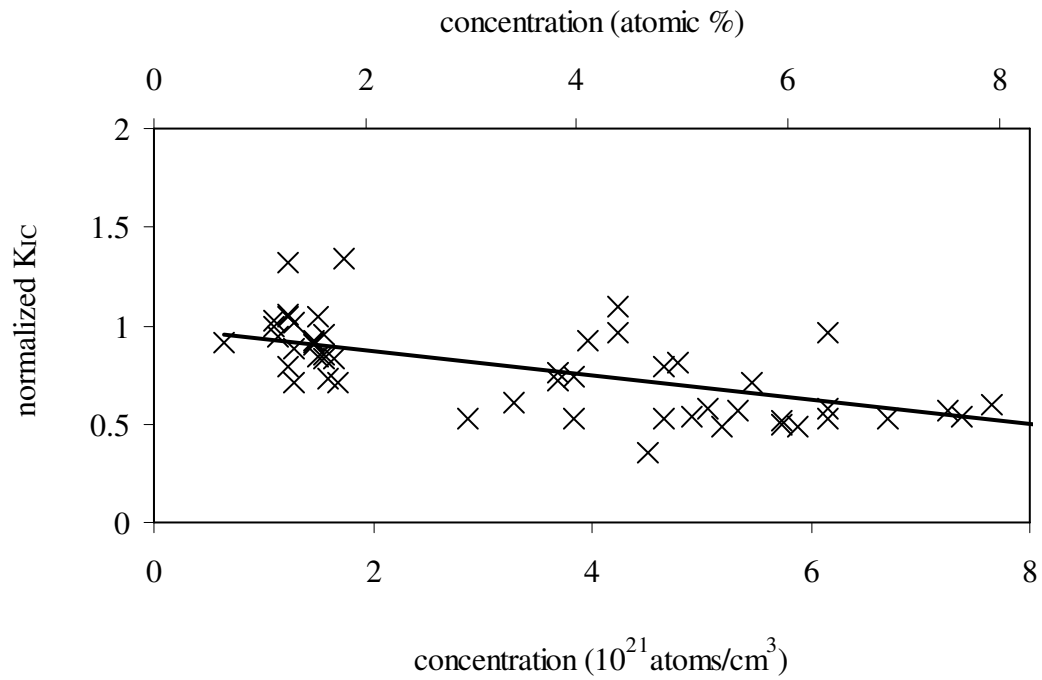


Figure 4.10(a): Normalized K_{IC} plotted as a function of P impurity concentration.

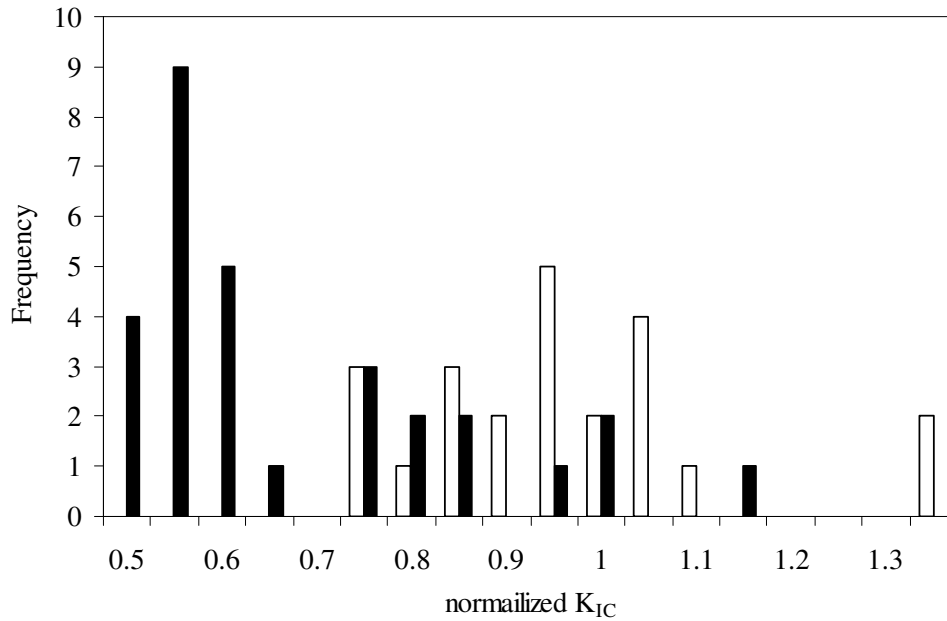


Figure 4.10(b): Normalized K_{IC} frequency plot for P impurity. Filled columns represent impurity concentration $< 2 \times 10^{21}$ atoms/cm³ and unfilled columns represent impurity concentration $> 2 \times 10^{21}$ atoms/cm³.

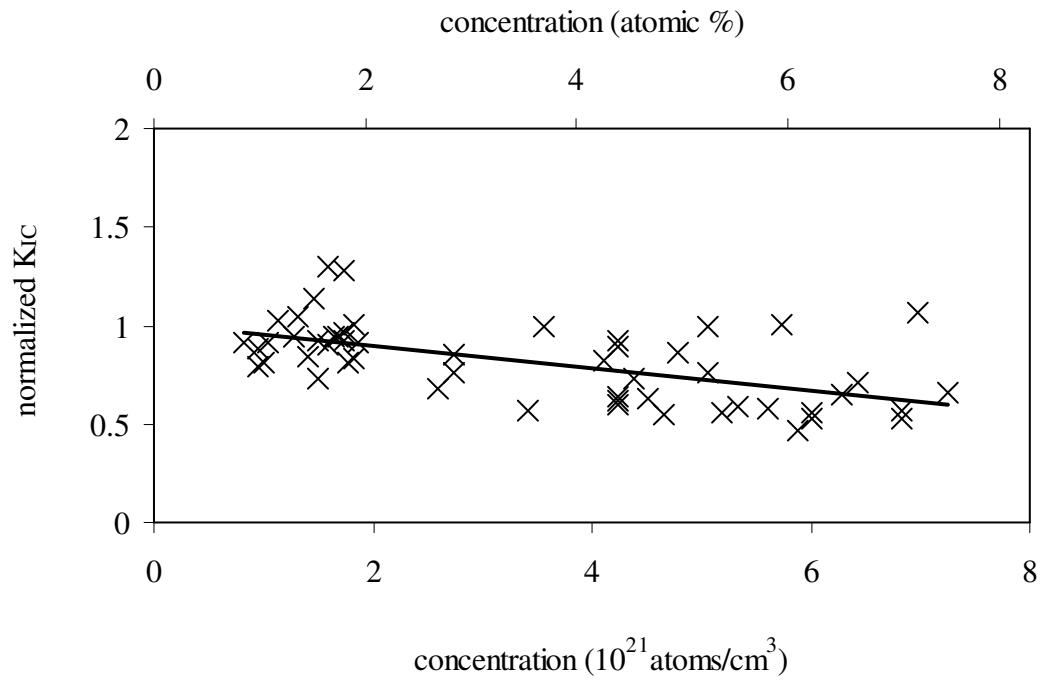


Figure 4.11(a): Normalized K_{IC} plotted as a function of Si impurity concentration.

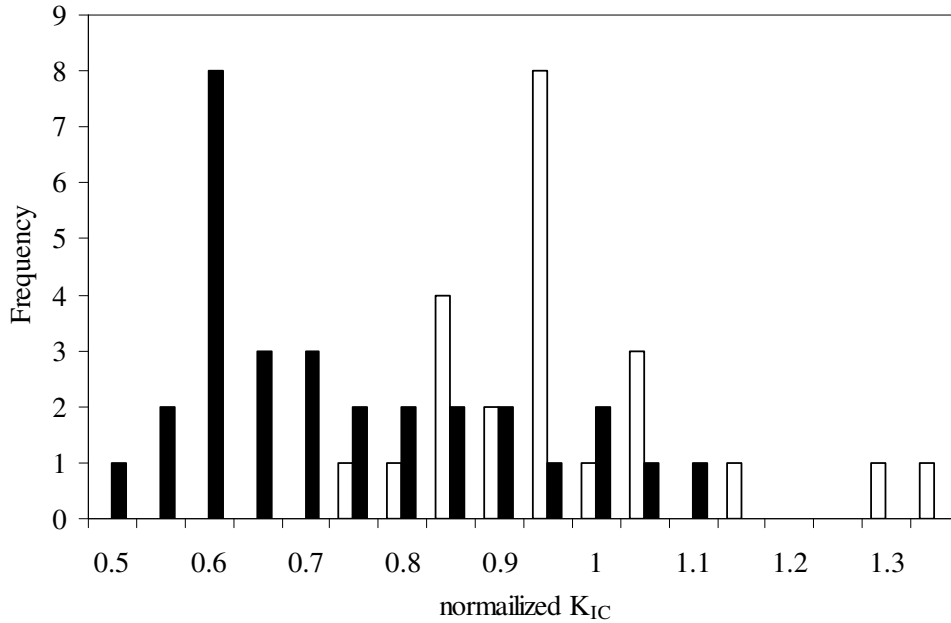


Figure 4.11(b): Normalized K_{IC} frequency plot for Si impurity. Filled columns represent impurity concentration < 2 × 10²¹ atoms/cm³ and unfilled columns represent impurity concentration > 2 × 10²¹ atoms/cm³.

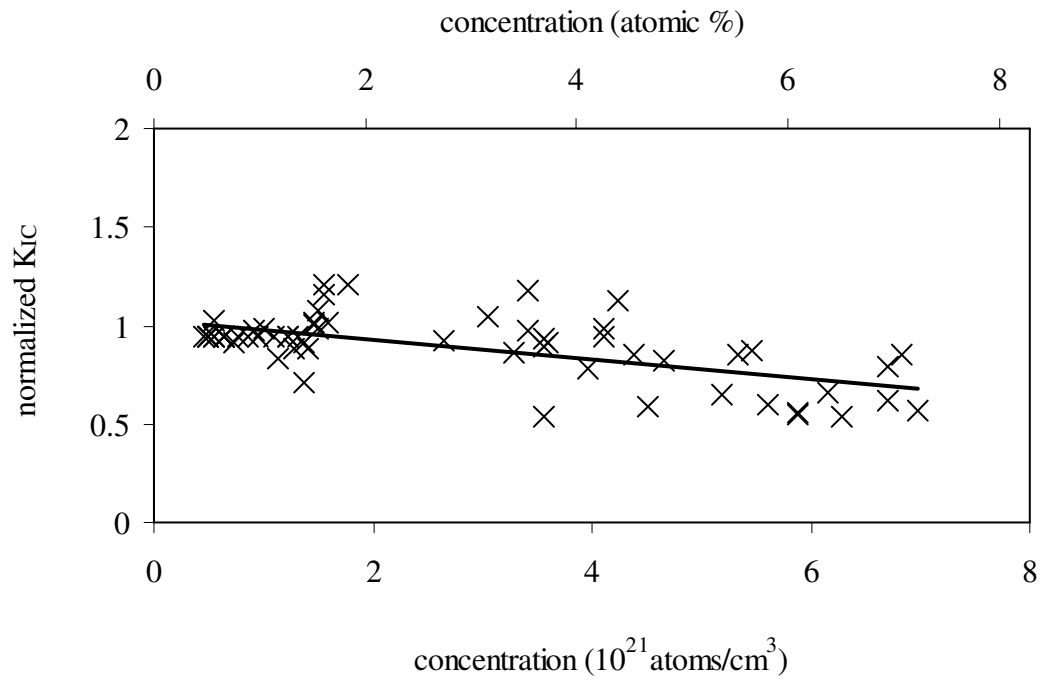


Figure 4.12(a): Normalized K_{IC} plotted as a function of C impurity concentration.

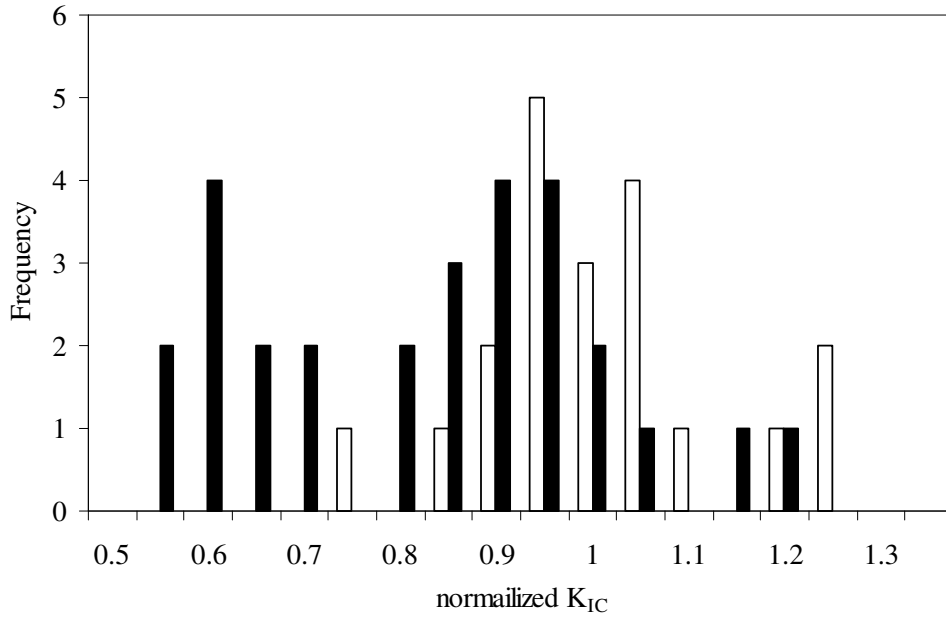


Figure 4.12(b): Normalized K_{IC} frequency plot for C impurity. Filled columns represent impurity concentration $< 2 \times 10^{21}$ atoms/cm³ and unfilled columns represent impurity concentration $> 2 \times 10^{21}$ atoms/cm³.

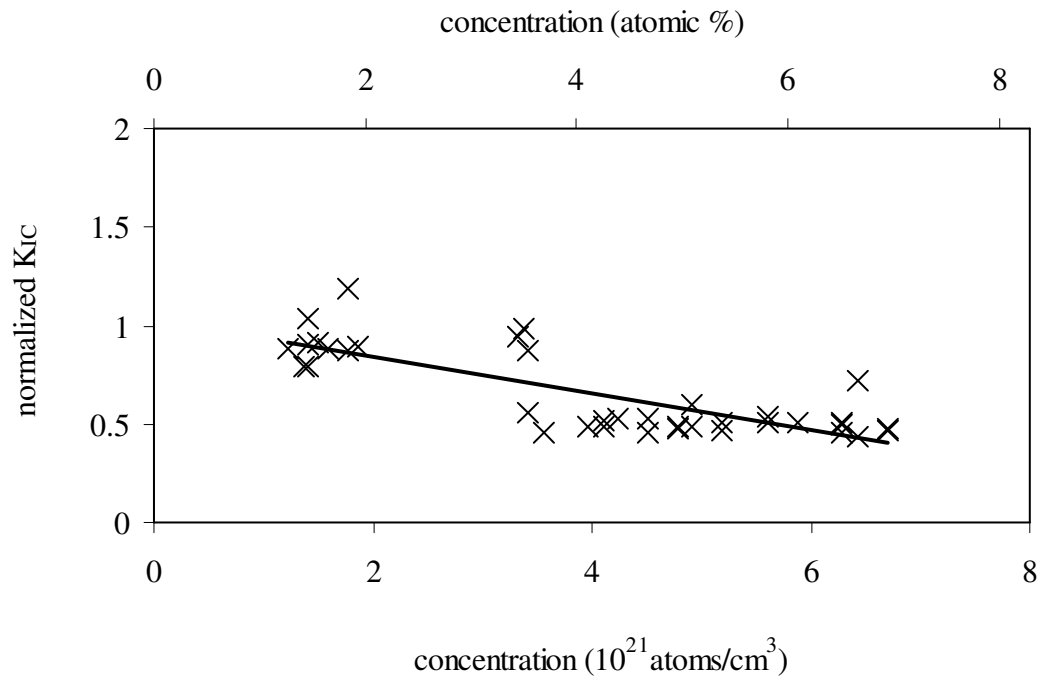


Figure 4.13(a): Normalized K_{IC} plotted as a function of H impurity concentration. The atomic percentage is defined as the number of H atoms relative to the total number of atoms in the sample.

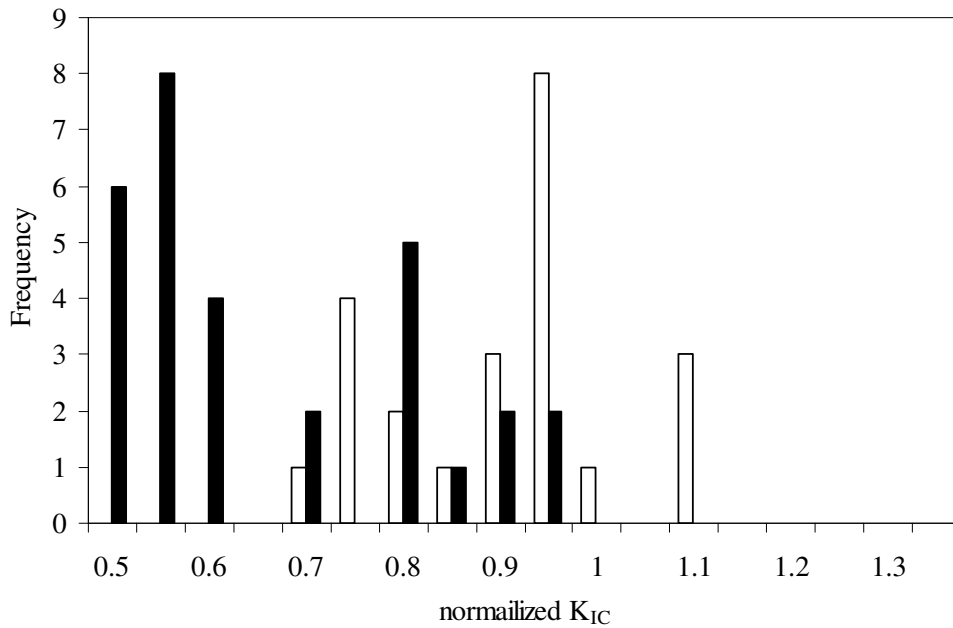


Figure 4.13(b): Normalized K_{IC} frequency plot for H impurity. Filled columns represent impurity concentration $< 2 \times 10^{21}$ atoms/cm³ and unfilled columns represent impurity concentration $> 2 \times 10^{21}$ atoms/cm³.

The impurity effects on K_{IC} of doped SiC at low concentration can be explained by the transition from decohesion to dislocation nucleation. All impurities in our studies decreased both the decohesion and slip resistance. However, it was found that the transition is controlled by the relative changes in $\Delta\Gamma_d$ and $\Delta\Gamma_s$. Figure 4.14(a) plots the average normalized K_{IC} , by K_{IC} of pure SiC, as a function of the ratio between the maximum $\Delta\Gamma_d$ divided by the maximum $\Delta\Gamma_s$ for all possible impurity sites ($\Delta\Gamma_s^{\max} / \Delta\Gamma_d^{\max}$). Based on $\Delta\Gamma_s^{\max} / \Delta\Gamma_d^{\max}$, the impurities can be roughly divided into two groups. The first group includes N, P, Si and H, with a $\Delta\Gamma_s^{\max} / \Delta\Gamma_d^{\max}$ ratio smaller than 1 and the second one B, C, and Al, with a ratio greater than 1. Given that pure SiC is brittle at low temperature, with N, P, Si or H at the crack tip, the crack tends to cleave on the shuffle set of the (1 1 1) plane than to nucleate dislocations because $\Delta\Gamma_d^{\max}$ is larger than $\Delta\Gamma_s^{\max}$, resulting in lower K_{IC} . In contrast, with Al, B and C at the crack tip, dislocation nucleation becomes more favorable. It can also be observed in figure 4.14(a) that a higher $\Delta\Gamma_s^{\max} / \Delta\Gamma_d^{\max}$ correlates to a higher K_{IC} at impurity concentration $< 2 \times 10^{21}$ atoms/cm³.

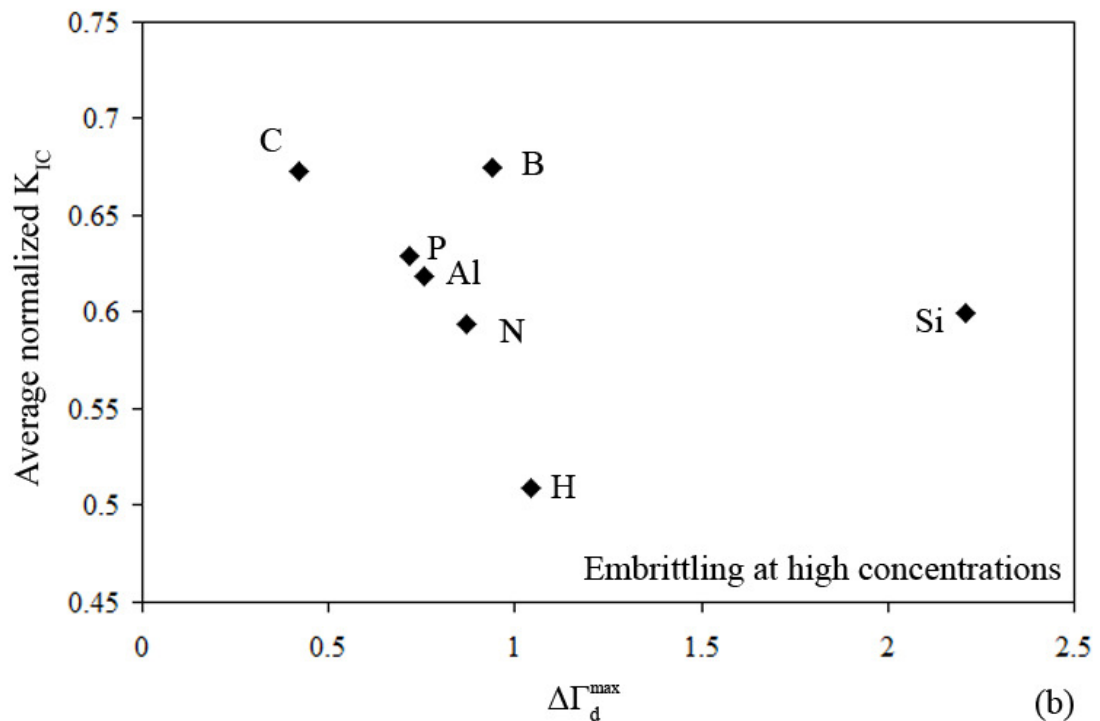
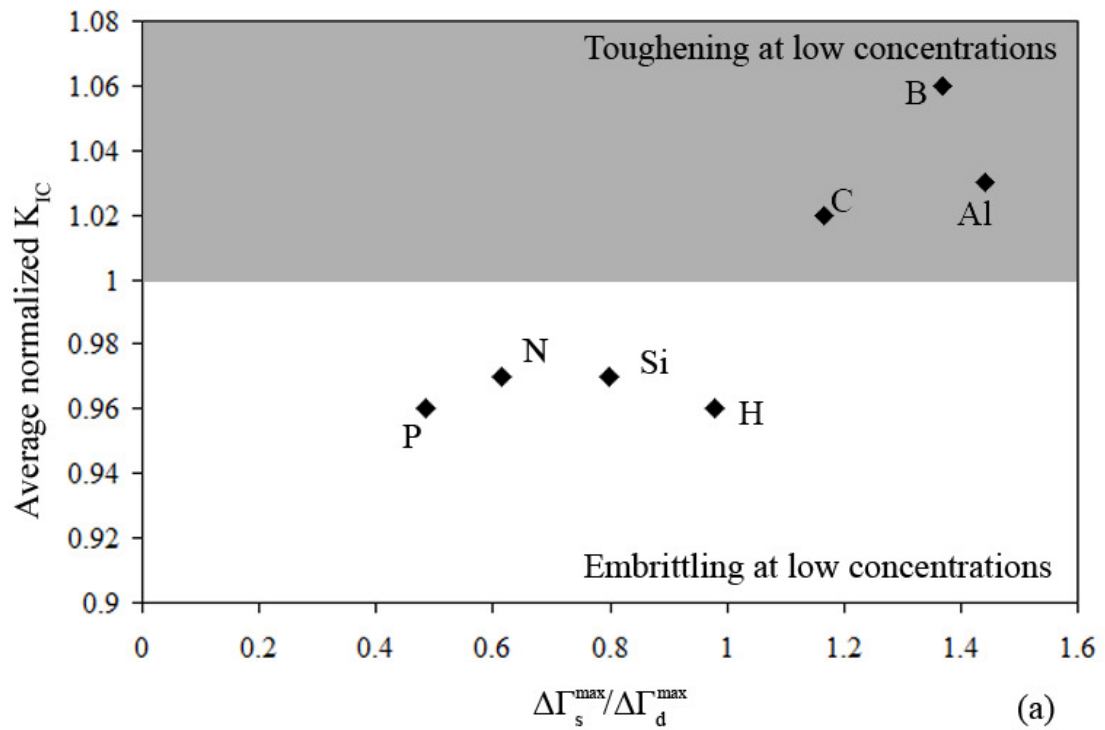


Figure 4.14: (a) plots the average normalized K_{IC} , by K_{IC} of pure SiC, as a function of $\Delta\Gamma_s^{\max}/\Delta\Gamma_d^{\max}$ of all possible impurity sites for low impurity concentration $< 2 \times 10^{21}$ atoms/cm³. The impurities with a smaller $\Delta\Gamma_s^{\max}/\Delta\Gamma_d^{\max}$ ratio tend to embrittle SiC. (b)

plots the average normalized K_{IC} , by K_{IC} of pure SiC, as a function of $\Delta\Gamma_d^{\max}$ of all possible impurity sites for high impurity concentration $> 6 \times 10^{21}$ atoms/cm³. All impurities embrittle SiC at high concentration.

Unlike at low impurity concentration, all impurities embrittle SiC at concentration $> 6 \times 10^{21}$ atoms/cm³, with the average normalized K_{IC} decreases by 50 to 70 %. As shown in figure 4.14(b), the average K_{IC} seems to decrease with $\Delta\Gamma_d^{\max}$, suggestion that the crack tip response is governed the change in decohesion resistance due to impurity effects. We hypothesize with increasing impurity concentration, the controlling crack tip mechanism undergoes transition from dislocation kink nucleation to dislocation kink propagation. At low concentration, impurities always decrease the resistance for dislocation kink nucleation as they lower the slip resistance. However, with increasing concentration, the propagation of dislocation is retarded by impurities, resulting an increase in dislocation kink propagation resistance. Eventually, dislocation kink nucleated from the crack tip becomes immobile with further addition of impurities and the plasticity mechanism is shut off. Thus, the crack tip is governed by decohesion.

To test our hypothesis on the effect of impurity concentration on dislocation glide, we performed empirical based atomistic simulations to estimate the critical shear stress at which dislocation starts gliding as a function of boron concentration. The simulations were performed using LAMMPS [21] with Devenathan et al. potential [16] and SBSA as described previously. The simulation cell was a fully periodic 3C-SiC crystal with [-1 1 0], [1 1 1] and [-1 -1 2] aligned with the X, Y and Z directions respectively. The size of the simulation box is shown in figure 4.15, with a 5 Å vacuum layer in the Y direction. A vertical plane of atoms was removed from the

top half of the crystal to create an edge dislocation gliding on the (1 1 1) plane in [-1 1 0] direction. Force boundary conditions were applied to the atoms along the Y boundaries. Stresses were computed with the virial theorem. The size of the simulation box was tested to ensure the convergence of the critical shear stress. To minimize computational expense, the impurities were placed in a 3 dimensional square array within the material based on impurity concentration. The SBSA was employed to incorporate the impurity effects on slip in the simulations. The critical shear stresses at which dislocation starts gliding are plotted as a function of impurity concentration in figure 4.16. The critical shear stress first decreases slightly as a function of concentration up to 1×10^{21} atom/cm³, a result of decrease in dislocation kink nucleation resistance. Then it increases up to 7.5 GPa at concentration = 7×10^{21} atom/cm³ due to increase in dislocation kink propagation resistance. This softening and hardening mechanism dependent on impurity concentration is also observed in metal [82,83].

The present work is the first attempt to study the K_{IC} under the influence of different impurities and impurity concentration combining first principles and empirical simulations. While there is no comparison for impurity effects on K_{IC} of single crystalline SiC available, our findings are in qualitative agreement with experimental studies on polycrystalline SiC, where C is likely to enhance plasticity at the crack tip and other impurities embrittle SiC by reducing cohesive surface energy [84,85].

Finally, because of the inaccuracies of the empirical potential, a significant disconnect can exist between the simulation results and real-world SiC behavior. First,

we successfully employed the SBSA approach to match the empirical simulation result for cleavage of pure SiC with our prior KSDFT result. Taking the KSDFT predictions of γ_{us} to be representative of real SiC, it seems that the empirical potential accurately predicts dislocation nucleation on the glide set but underpredicts the occurrence of dislocation nucleation on the shuffle set. Furthermore, plasticity of pure SiC is controlled by dislocation kink nucleation in our empirical potential-based simulation. However, it is possible that kink propagation is the rate-limiting step for dislocation glide motion in SiC [86]. Assembling all pieces of this work, we conclude that while impurities enhance dislocation nucleation in real SiC, the improvement in fracture toughness is rather limited because of the high dislocation kink propagation resistance, due to impurities or the crystal itself. We suggest that a larger improvement in fracture toughness is possible for other ceramics [87] and BCC metals [88] through doping, if dislocation kink nucleation is the rate-limiting step.

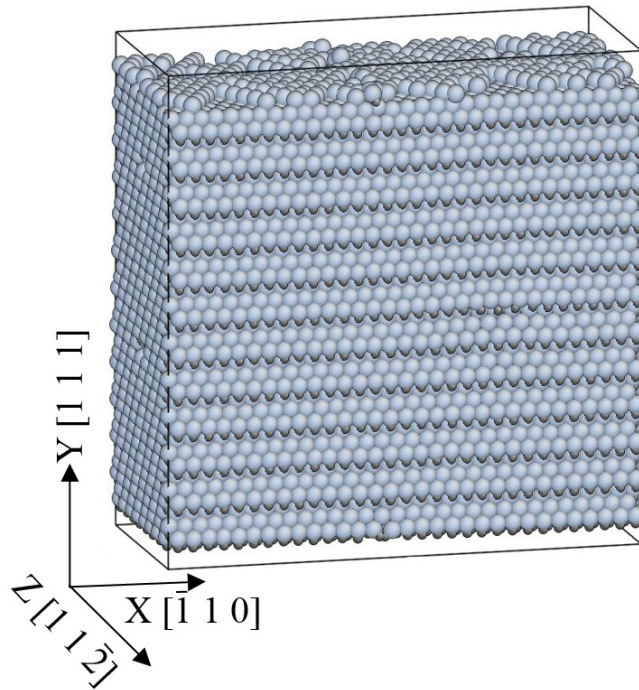


Figure 4.15: Illustration of the simulation cell for computing the critical shear stress at which dislocation starts gliding.

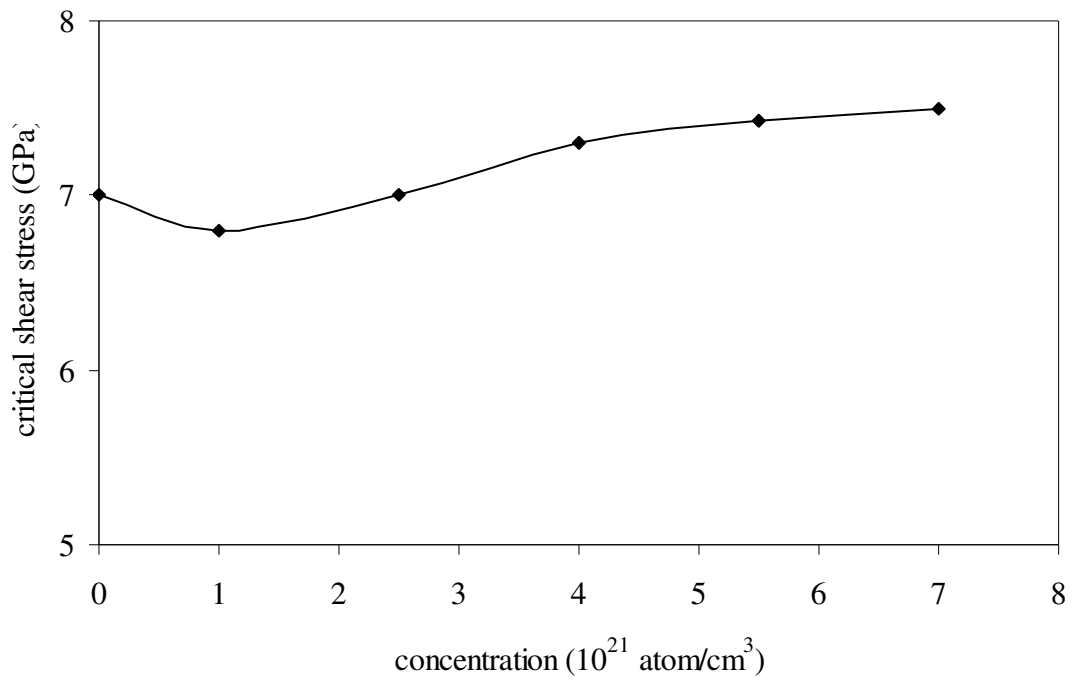


Figure 4.16: Plot of the critical shear stress at which dislocation starts gliding as a function of boron concentration.

4.7 Summary

The utility of SiC as a structural material has been limited by its low fracture toughness. Our work sought to better understand the impurity effects on SiC crack tip mechanisms in order to accurately predict catastrophic failure events and to improve its fracture toughness. We took a 2 step approach to predict the impurity effects on K_{IC} of SiC: (1) We first characterized SiC's decohesion and slip resistance by computing the impurity effects on $\Delta\Gamma_d$ and $\Delta\Gamma_s$ for the most probable cleavage and dislocation glide plane. Six substitution impurities Al, B, C, N, P and Si and one interstitial impurity H were examined. All impurities increase the tendency towards decohesion and most impurities increase the tendency for slip. (2) Next, the impurities effect on K_{IC} of SiC was studied by performing atomistic simulations with Devanathan et al. empirical potential with SBSA to replicate the impurity effects on decohesion and. Our results show that K_{IC} depends on the type and concentration of impurity near the crack tip. For N, P, Si and H impurities, K_{IC} decreases monotonically as impurity concentration increases, due to impurity enhanced decohesion over dislocation nucleation. Interestingly, samples with Al, B and C exhibit a non-monotonic effect of impurity concentration. At concentration $< 2 \times 10^{21}$ atoms/cm³, K_{IC} is higher relative to pure SiC and turns lower at high concentration. This phenomenon is attributed to the competition of two mechanisms governing dislocation motion. At low impurity concentration, impurities decrease dislocation kink nucleation resistance; at high concentration, dislocation kink propagation resistance increases because impurities

retard kink propagation. We further illustrated this point by computing the critical shear stress as a function of impurity concentration.

In summary, N, P, Si and H impurities always have embrittling effect, while Al, B and C can have embrittling or toughening effect depending on impurity concentration. We conclude that the improvement in fracture toughness of real SiC through doping is limited because the rate determining step of dislocation glide is likely to be controlled by dislocation kink propagation. Doping is expected to increase the fracture toughness more significantly for ceramics and metals whose plasticity response is governed by dislocation kink nucleation. By combining first principles-based calculations and empirical-based atomistic simulations, our studies built a foundation for understanding environmental and impurity effects on the crack tip mechanisms of SiC using physics based model and unveiled new means to improve fracture toughness through doping.

BIBLIOGRAPHY

- [1] R. Naslain and F. Christin. SiC-matrix composite materials for advanced jet engines. *Materials Research Society Bulletin*, 28(9):654-658, 2003.
- [2] M. Belmonte. Advanced ceramic materials for high temperature applications. *Advanced Engineering Materials*, 8(8):693-703, 2006.
- [3] C. M. Grondahl and T. Tsuchiya. Performance benefit assessment of ceramic components in an MS9001FA gas turbine. *Journal of Engineering for Gas Turbines and Power*, 123(3):513-519, 2001.
- [4] K. Shenai K, R. S. Scott RS, and B. J. Baliga. Optimum semiconductors for high-power electronics. *IEEE Transactions on Electron Devices*, 36(9):1811-1823, 1989.
- [5] J. B. Casady and R. W. Johnson. Status of silicon carbide (SiC) as a wide-bandgap semiconductor for high-temperature applications: a review. *Solid-State Electronics*, 39(10):1409-1422, 1996.
- [6] J. L. Henshall, D. J. Rowcliffe, and J. W. Edington. Fracture toughness of single-crystal silicon carbide. *Journal of The American Ceramic Society*, 60:373-375, 1977.
- [7] J. J. Petrovic and R. B. Roof. Fracture toughness of a beta-SiC whisker. *Journal of The American Ceramic Society*, 67(10):C219-220, 1984.
- [8] R. Stevens. Dislocation movement and slip systems in β -SiC. *Journal of Materials Science*, 5:474-477, 1970.
- [9] J. L. Demenet et al. Dislocations in 4H- and 3C-SiC single crystals in the brittle regime. *Physics Status Solidi C*, 10(1):64-67, 2013.
- [10] J. L. Demenet, X. Milhet, and J. Rabier. TEM observations of the coexistence of perfect and dissociated dislocations in SiC under high stress. *Physics Status Solidi C*, 6:1987-1991, 2005.
- [11] P. Pirouz, A. V. Samant, and M. H. Hong. On temperature dependence of deformation mechanism and the brittle-ductile transition in semiconductors. *Journal of Materials Research*, 14(7):2783-2793, 1999.
- [12] G. H. Campbell, B. J. Dalgleish, and A. G. Evans. Brittle-to-ductile transition in silicon carbide. *Journal of The American Ceramic Society*, 72(8):1402-1408, 1989.

-
- [13] H. Kikuchi et al. Brittle dynamic fracture of crystalline cubic silicon carbide via molecular dynamics simulation. *Journal of Applied Physics*, 98:103524, 2005.
- [14] J. Riedle, P. Gumbsch, and H. F. Fischmeister. Cleavage anisotropy in tungsten single crystals. *Physical Review Letter*, 76(19):3594-3597, 1996.
- [15] Y. Umeno, Y. Kinoshita, and T. Kitamura. Ab initio DFT simulation of ideal shear deformation of SiC polytypes. *Modelling and Simulation in Materials Science and Engineering*, 15:27-37, 2007.
- [16] R. Devanathan, T. Diaz de la Rubia, and W. J. Weber. Displacement threshold energies in β -SiC. *Journal of Nuclear Materials*, 253:47-53, 1998.
- [17] P. Erhart and K. Albe. Analytical potential for atomistic simulations of silicon, carbon, and silicon carbide. *Physical Review B*, 71:035211, 2005.
- [18] J. Tersoff. Modeling solid-state chemistry: Interatomic potentials for multicomponent systems. *Physical Review B*, 39:5566-5568, 1989.
- [19] H. Kleykamp and G. Schumacher. The constitution of the silicon-carbon system. *Berichte der Bunsengesellschaft für physikalische Chemie*, 97:799-804, 1993.
- [20] R. Devanathan and W. J. Weber. Displacement energy surface in 3C and 6H SiC. *Journal of Nuclear Materials*, 278:258-265, 2000.
- [21] S. Plimpton. Fast Parallel Algorithms for Short-Range Molecular Dynamics. *Journal of Computational Physics*, 117:1-19, 1995.
- [22] T. Schneider and E. Stoll. Molecular-dynamics study of a three-dimensional one-component model for distortive phase transitions. *Physical Review B*, 17(3):1302-1322, 1978.
- [23] J. R. Rice and G. Beltz. The activation energy for dislocation nucleation at a crack. *Journal of the Mechanics and Physics of Solids*, 42:333-360, 1994.
- [24] J. Li. AtomEye: an efficient atomistic configuration viewer. *Modelling and Simulation in Materials Science and Engineering*, 11:173-177, 2003.
- [25] A. Mattoni, M. Ippolito, and L. Colombo. Atomistic modeling of brittleness in covalent materials. *Physical Review B*, 76:224103, 2007.
- [26] J. E. Sinclair. The influence of the interatomic force law and of kinks on the propagation of brittle cracks. *Philosophical Magazine*, 31:647-671, 1975.
- [27] C. Thaulow, D. Sen, and M. J. Buehler. Atomistic study of the effect of crack tip ledges on the nucleation of dislocations in silicon single crystals at elevated temperature. *Materials Science and Engineering A*, 528:4357-4364, 2011.

-
- [28] A. N. Pilyankevich and V. F. Britun. Motion of partial dislocation in silicon carbide. *Physics Status Solidi A*, 82(2):449-457,1984.
- [29] S. Ha, M. Benamara, M. Skowronski, and H. Lendenmann. Core structure and properties of partial dislocations in silicon carbide p-i-n diodes. *Applied Physical Letters*, 83:4957-4959,2003.
- [30] A. A. Griffith. The phenomena of rupture and flow in solids. *Philosophical Transactions of the Royal Society of London Series A*, 221:163-198, 1921.
- [31] Z. Li and R. C. Bradt. The single-crystal elastic constants of cubic (3C) SiC to 1000°C. *Journal of Materials Science*, 22:2557-2559, 1987.
- [32] K. B. Tolpygo. Optical, elastic and piezoelectric properties of ionic and covalent crystals with the ZnS type lattice. *Soviet Physics-Solid State*, 2:2367-2376, 1961.
- [33] N. Bernstein and D. W. Hess. Lattice trapping barriers to brittle fracture. *Physics Review Letter*, 91(2):025501, 2003.
- [34] R. Perez and P. Gumbsch. An ab initio study of the cleavage anisotropy in silicon. *Acta Materialia*, 48:4517-4530, 2000.
- [35] T. Zhu, K. Gall, J. Li, A. Samanta and A. Leach. Temperature and strain-rate dependence of surface dislocation nucleation. *Physical Review Letters*, 100:025502, 2008.
- [36] T. R. Duncan and D. K. Wilsdorf. Shear stresses and strain energies of edge dislocations in anisotropic cubic crystals. *Journal of Applied Physics*, 38:313-322, 1967.
- [37] V. I. Yamakov et al. Investigation of crack tip dislocation emission in aluminum using multiscale molecular dynamics simulation and continuum modeling. *Journal of the Mechanics and Physics of Solids*, 65:35-53,2014.
- [38] D. H. Warner and W. A. Curtin. Origins and implications of temperature-dependent activation energy barriers for dislocation nucleation in face-centered cubic metals. *Acta Materialia*, 57:4267-4277, 2009.
- [39] L. D. Nguyen, K. L. Baker, and D. H. Warner. Atomistic predictions of dislocation nucleation with transition state theory. *Physical Review B*, 84:024118, 2011.
- [40] S. Ryu, K. Kang, and W. Cai. Entropic effect on the rate of dislocation nucleation. *Proceedings of the National Academy of Sciences of the United States of America*, 108:5174-5178, 2011.

-
- [41] L. M. Dupuy, E. B. Tadmor, R. E. Miller, and R. Phillips. Finite-temperature quasicontinuum: molecular dynamics without all the atoms. *Physical Review Letters*, 95:060202, 2005.
- [42] M. Zhang, H. Hobgood, J. L. Demenet, and P. Pirouz. Transition from brittle fracture to ductile behavior in 4H-SiC. *Journal of Materials Research*, 18(5):1087-1095, 2003.
- [43] P. Gumbsch, J. Riedle, A. Hartmaier, and H. F. Fischmeister. Controlling factors for the brittle-to-ductile transition in tungsten single crystals. *Science*, 282:1293-1295, 1998.
- [44] R. Peierls. The size of a dislocation. *Proceedings of the Physical Society*, 52:34-37, 1940.
- [45] J. R. Rice. Dislocation nucleation from a crack tip: an analysis based on the Peierls concept. *Journal of the Mechanics and Physics of Solids*, 40:237-271, 1992.
- [46] A. K. Nair, D. H. Warner, and R. G. Hennig. Coupled quantum-continuum analysis of crack tip processes in aluminum. *Journal of the Mechanics and Physics of Solids*, 59:2476-2487, 2011.
- [47] R. J. Zamora, A. K. Nair, R. G. Hennig, and D. H. Warner. Ab initio prediction of environmental embrittlement at a crack tip in aluminum. *Physical Review B*, 86:060101, 2012.
- [48] K. W. K. Leung, Z. L. Pan, and D. H. Warner. Atomistic-based predictions of crack tip behavior in silicon carbide across a range of temperatures and strain rates. *Acta Materialia*, 77:324-334, 2014.
- [49] S. Kohlhoff, P. Gumbsch, and H. F. Fischmeister. Crack propagation in b.c.c. crystals studied with a combined finite-element and atomistic model. *Philosophical Magazine A*, 64(4):851-878, 1991.
- [50] G. Lu, E. B. Tadmor, and E. Kaxiras. From electrons to finite elements: A concurrent multiscale approach for metals. *Physics Review B*, 73:024108, 2006.
- [51] W. Kohn and L. J. Sham. Self-consistent equations including exchange and correlation effects. *Physical Review*, 140(4A):A1133-1138, 1965.
- [52] V. M. Born and R. Oppenheimer. Zur Quantentheorie der Molekeln. *Annalen der Physik*, 20:457-484, 1927.
- [53] G. Kresse and J. Hafner. Ab initio molecular dynamics for open-shell transition metals. *Physical Review B*, 48(17):13115, 1993.

-
- [54] D. Vanderbilt. Soft self-consistent pseudopotentials in a generalized eigenvalue formalism. *Physical Review B*, 41(11):7892-7895, 1990.
- [55] G. Kresse and J. Hafner. Norm-conserving and ultrasoft pseudopotentials for first-row and transition elements. *Journal of Physics: Condensed Matter*, 6:8245-8257, 1994.
- [56] J. Perdew et al. Atoms, molecules, solids, and surfaces: Applications of the generalized gradient approximation for exchange and correlation. *Physical Review B*, 46(11):6671-6687, 1992.
- [57] G. Kresse and J. Hafner. Ab initio molecular dynamics for liquid metals. *Physical Review B*, 47(1):558-561, 1993.
- [58] G. Kresse and J. Hafner. Ab initio molecular-dynamics simulation of the liquid-metal-amorphous-semiconductor transition in germanium. *Physical Review B*, 49(20):14251-14268, 1994.
- [59] G. Kresse and J. Furthmüller. Efficiency of ab-initio total energy calculations for metals and semiconductors using a plane-wave basis set. *Computational Materials Science*, 6:15-50, 1996.
- [60] G. Kresse and J. Furthmüller. Efficient iterative schemes for ab initio total-energy calculations using a plane-wave basis set. *Physical Review B*, 54(16):11169-11186, 1996.
- [61] M. Methfessel and A. T. Paxton. High-precision sampling for Brillouin-zone integration in metals. *Physical Review B*, 40(6):3616-3621, 1989.
- [62] E. K. K. Abavare, J. I. Iwata, A. Yaya, and A. Oshiyama. Surface energy of Si(110)- and 3C-SiC(111)-terminated surfaces. *Physics Status Solidi B*, 251(7):1408-1415, 2014.
- [63] P. Käckell, J. Furthmüller, and F. Bechstedt. Ab initio calculations of the reconstructed (100) surfaces of cubic silicon carbide. *Applied Surface Science*, 104/105:45-48, 1996.
- [64] L. E. Shilkrot, R. E. Miller, and W. A. Curtin. Coupled atomistic and discrete dislocation plasticity. *Physics Review Letter*, 89(2):025501, 2002.
- [65] W. Humphrey, A. Dalke, and K. Schulten. VMD: Visual molecular dynamics. *Journal of Molecular Graphics*, 14:33-38, 1996.

-
- [66] J. H. Rose, J. Ferrante, and J. R. Smith. Universal binding energy curves for metals and bimetallic interfaces. *Physical Review Letter*, 47(9):675-678, 1981.
- [67] S. Kiani et al. Dislocation glide-controlled room-temperature plasticity in 6H-SiC single crystals. *Acta Materialia*, 80:400-406, 2014.
- [68] J. Kimmel et al. Evaluation of CFCC liners with EBC after field testing in a gas turbine. *Journal of the European Ceramic Society*, 22:2769-2775, 2002.
- [69] F. Demichelis, C. F. Pirri, and E. Tresso. Influence of doping on the structural and optoelectronic properties of amorphous and microcrystalline silicon carbide. *Journal of Applied Physics*, 72(4):1327-1333, 1992.
- [70] C. Wang et al. Effects of doping atoms on the generalized stacking-fault energies of Mg alloys from first-principles calculations. *Scripta Materialia*, 69:445-448, 2013.
- [71] U. V. Waghmare, V. Bulatov, E. Kaxiras, and M. S. Duesbery. Microalloying for ductility in molybdenum disilicide. *Materials Science and Engineering*, A261:147-157, 1999.
- [72] C. B. Geller et al. A computational search for ductilizing additives to Mo. *Scripta Materialia*, 52:205-210, 2005.
- [73] D. E. Jiang and E. A. Carter. First principles assessment of ideal fracture energies of materials with mobile impurities: implications for hydrogen embrittlement of metals. *Acta Materialia*, 52:4801-4807, 2004.
- [74] A. Gali. Ab initio study of nitrogen and boron substitutional impurities in single-wall SiC nanotubes. *Physical Review B*, 73:245415, 2006.
- [75] R. Rurali et al. First-principles study of n-type dopants and their clustering in SiC. *Applied Physics Letters*, 82:4298-4300, 2003.
- [76] A. Fukumoto. First-principles calculations of p-type impurities in cubic SiC. *Physical Review B*, 53(8):4458-4461, 1996.
- [77] J. Perdew et al. Atoms, molecules, solids, and surfaces: Applications of the generalized gradient approximation for exchange and correlation. *Physical Review B*, 46(11):6671-6687, 1992.
- [78] S. Hong and M. Y. Chou. Effect of hydrogen on the surface-energy anisotropy of diamond and silicon. *Physical Review B*, 57(11):6262-6265, 1998.

-
- [79] V. N. Erofeev, V. I. Nikitenko, and V. B. Osvenskii. Effect of impurities on the individual dislocation mobility in silicon. *Physics Status Solidi*, 35:79-88, 1969.
- [80] J. R. Patel, L. R. Testardi, and P. E. Freeland. Electronic effects on dislocation velocities in heavily doped silicon. *Physical Review B*, 13(8):3548-3557, 1976.
- [81] P. K. Sitch et al. Ab initio investigation of the dislocation structure and activation energy for dislocation motion in silicon carbide. *Physical Review B*, 52(7):4951-4955, 1995.
- [82] D. R. Trinkle and C. Woodward. The chemistry of deformation: how solutes soften pure metals. *Science*, 310:1665-1667, 2005.
- [83] R. Kirchheim. Solid solution softening and hardening by mobile solute atoms with special focus on hydrogen. *Scripta Materialia*, 67:767-770, 2012.
- [84] Y. Matsuda et al. Fracture properties of hydrogenated amorphous silicon carbide thin films. *Acta Materialia*, 60:682-691, 2012.
- [85] R. H. Jones et al. Stress-corrosion cracking of silicon carbide fiber / silicon carbide composites. *Journal of The American Ceramic Society*, 83(8):1999-2005, 2000.
- [86] A. T. Blumenau et al. Straight and kinked 90 partial dislocation in diamond and 3C-SiC. *Journal of Physics: Condensed Matter*, 14:12741-12747, 2002.
- [87] W. Cai et al. Intrinsic mobility of a dissociated dislocation in silicon. *Physics Review Letter*, 84(15):3346-3349, 2000.
- [88] M. Wen and H. W. Ngan. Atomistic simulation of kink-pairs of screw dislocations in body-centered cubic iron. *Acta Materialia*, 48:4255-4265, 2000.